# Production of $\Sigma^0$ in $\sqrt{s} = 91.2\ GeV\ q\overline{q}$ events at LEP

by

Christopher Kenneth Legan

A dissertation submitted to the graduate faculty
in partial fulfillment of the requirements for the degree of
DOCTOR OF PHILOSOPHY

Major: High Energy Physics
Major Professor: H. Bert Crawley

Iowa State University
Ames, Iowa
1997

Graduate College
Iowa State University

This is to certify that the Doctoral dissertation of

Christopher Kenneth Legan

has met the dissertation requirements of Iowa State University

Major Professor

For the Major Program

For the Graduate College

*This thesis is dedicated to my family - Christine, Olivia and Sophie - and the grandparents of our children*

## TABLE OF CONTENTS

# LIST OF FIGURES

# LIST OF TABLES

# ABSTRACT

This thesis presents a measurement of one of the three isospin states of the $J^P = \frac{1}{2}^+$ octet $\Sigma$ baryons, the $\Sigma^0$. In addition, the analysis yields the first differential cross-section measurement of the $\Sigma^0$ hyperon in $e^+e^- \to q\bar{q}$ events. The unique particle identification capabilities of the DELPHI detector at LEP are used to obtain an increased efficiency by extending the standard $\Lambda$ –finding algorithm.

The average number of $\Sigma^0$'s produced per $Z^0$ decay is calculated to be

$$N(\Sigma^0)/Z^0_{had} = 0.101 \pm 0.008(\text{stat}) \pm 0.014(\text{syst}) \pm 0.007(\text{extrap}) \qquad (0.1)$$

The measurement is about 30% above the prediction of the JETSET model, but nevertheless is compatible with JETSET within 2 $\sigma$. Comparison with ARGUS results at $\sqrt{s} = 10 GeV$ reveals similar levels of spin and strangeness suppression in hyperon production, within errors.

# 1 INTRODUCTION

*There is a theory which states that if ever anybody discovers exactly what the Universe is for and why it is here, it will instantly disappear and be replaced by something even more bizarre and inexplicable. There is another theory which states that this has already happened.*

Douglas Adams, *Hitchhiker's Guide to the Galaxy*

*A witty saying proves nothing.*

Voltaire (1694-1778)

Measuring the production rates of baryons in general, and strange baryons in particular, is important in order to understand the underlying fragmentation process in $Z^0 \to q\bar{q}$ events. The fragmentation process transforms an initial set of partons into a final set of hadrons. It has not yet been understood from first principles, but only in terms of vaguely QCD-inspired models, with many issues unresolved. However, once a $q\bar{q}$ pair has been produced, the evolution into a hadronic final state follows the same basic rules independent of CM energy. As a consequence, the experience accumulated at LEP adds directly to the PEP/PETRA/TRISTAN programs. A number of different phenomonological models have been developed which aim for a good representation of existing data, plus a predictive power for properties not yet studied or results at higher energies.

The most widely used models are implemented in the simulation programs HERWIG (cluster fragmentation) [39] and JETSET (string fragmentation) [44]. The string model describes the hadronization as the fragmentation of a color string. The string is 1-dimensional, and represents the energy of the strong interaction between two partons. The physical picture is that of a color flux tube being stretched between the partons that were produced in hard QCD processes, with the gluon (which also has a color-charge) as the mediator of their interactions. The transverse dimensions of the tube are of typical hadronic sizes, roughly 1 fm. If the tube is assumed to be uniform along it's length, this leads to a confinement picture with a linearly rising potential. This is the unusual aspect of QCD which leads to the striking difference between QCD processes (such as the formation of hadrons during string fragmentation), and the much weaker and unconfined electroweak or gravitational interactions. The string has an energy density per unit length of $\sim$1GeV/fm. When the partons are separated spatially by a sufficient amount, it becomes energetically favorable to produce $q\bar{q}$ pairs, thus splitting the string. Occasionally the string can also break up via the production of a diquark-anti-diquark ($D\bar{D}$) pair. The diquarks can form a baryon-anti-baryon pair with neighboring quarks on either side of the string. This is called direct diquark fragmentation, and is shown in Fig. 1.1a. A related mechanism, termed popcorn production, allows $D\bar{D}$ pairs to overlap with other $q\bar{q}$ pairs in the string (see Fig 1.1b and 1.1c).

By contrast, the concept of cluster fragmentation offers a simple, local and universal description of hadronization. A cluster is ideally only characterized by its total mass and total flavor content, i.e. unlike a string it does not possess internal structure. This gives a compact description with few

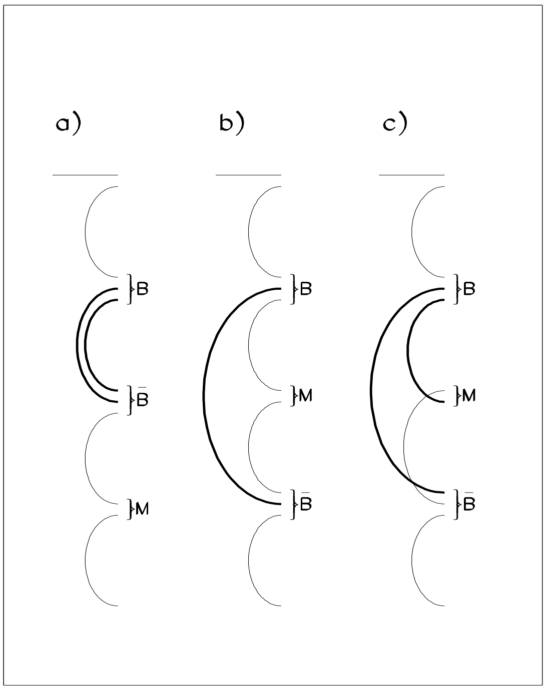

Figure 1.1 Schematic representation of baryon production in the string model. The top lines indicate primary quarks, the semi-circles $q\bar{q}$ pairs. Direct diquark fragmentation is shown in a), the popcorn mechanism is represented in b) and c) [21]

parameters. In the cluster model as implemented in HERWIG , there is only one production mode for baryons. According to the available phase space depending on the masses of the clusters and the produced hadrons, clusters can decay into one or two mesons or two baryons. There are no free parameters to control this particular process.

Most models treat baryon formation in the same spirit as meson formation, but maybe the underlying physics is quite different. Tuning of model parameters is attempted, but neither of the models mentioned above can simultaneously reproduce all observed features of baryon production for various flavor and spin content. Measurements performed both for LEP and for lower energy $e^+e^-$ machines show that the production of baryons with high spin and/or strangeness content is suppressed [2, 10, 11, 12]. However, the measurements are insufficient to constrain the models fully, and it is necessary to measure as many of the octet and decuplet baryon rates as possible, as well as their differential cross-sections. Since there are substantial differences between the predictions of the two models, a measurement of the hyperon production rates and their differential cross-sections offers a more complete picture to evaluate the merits of the different fragmentation schemes.

This thesis presents a measurement of one of the three isospin states of the $J^P = \frac{1}{2}^+$ octet $\Sigma$ baryons, the $\Sigma^0$. The $\Sigma^-$production in hadronic $Z^0$ decays has recently been measured by DELPHI eChristian. Both measurements are above the prediction of the JETSET model, but nevertheless are compatible with JETSET within 2 $\sigma$. In addition, this analysis yields the first differential cross-section measurement of the $\Sigma^0$ hyperon in $e^+e^- \to q\bar{q}$ events. The shape of the differential cross section is well described in JETSET . These results are to be considered a correction to, rather than an improvement of, the measurement of the inclusive $\Sigma^0$ production rate found in my previous analysis [8].

# 2 THE EXPERIMENT

This chapter describes the experimental setup of the Large Electron Positron (LEP) collider at CERN. The DELPHI detector, one of the four LEP experiments, is discussed in more detail after a short introduction to the LEP machine. Finally, a description of the DELPHI online and offline systems is given.

## 2.1 The LEP Collider

The LEP storage ring, with a circumference of about 26.7 km, is installed in the LEP tunnel. LEP lies 50 to 175 meters below the surface, has a diameter of 3.80 m, and straddles the French (Pays de Gex) - Swiss (Canton Genève) border[36]. A schematic map of the local area is given in Fig. 2.1. The LEP ring consists basically of a beam pipe, magnets, acceleration sections and their power supplies. The magnets either bend or focus the electron beam, while the acceleration sections, consisting of 128 radio frequency cavities, provide the energy for the acceleration of the electrons and positrons. In total, LEP100 contained 3 392 dipole magnets (for bending), and 876 quadrupole, 520 sextupole and 700 correction magnets (for focussing). Since the electrons and positrons have opposite electric charge and equal mass, they can circulate in opposite directions in a single beam pipe with the same arrangement of focussing and bending magnets. All of these LEP components are aligned to an accuracy of 0.1 mm, and so precise is the machine's energy measured that LEP can detect the orbit of the moon, heavy rainfall, and changing water levels in Lake Geneva. Even the departure of the TGV from Geneva bound for Paris does not escape LEP's attention.

October 1995 signalled the end of LEP100, which was the period of data-taking relevant to this analysis. The energy of the electrons and positrons in the LEP100 phase was near 45.6 GeV ($\sqrt{s} = m_{Z^0}$). Starting in 1996, the center of mass energy of LEP was increased up to 180 GeV in order to produce $W^+W^-$ pairs. With a scheduled integrated luminosity of 500 pb$^{-1}$ roughly 10 000 $W^\pm$ pairs are expected per experiment. The main physics goals are investigations of the properties of the $W^\pm$ boson (e.g. a precise measurement of its mass), and searches for new physics (e.g. Higgs or supersymmetric particles). A serious problem for LEP200 is the energy consumption of the ring. Synchrotron radiation results in an expected energy loss of about 38 MW running in the eight bunch mode. This corresponds to roughly 10% of the production of a modern power station. In order to optimize the acceleration sections of LEP, the conventional radio-frequency (RF) cavities are being replaced with superconducting RF cavities. To achieve 96 GeV per beam in 1998, the total number of acceleration sections will be increased to 324.

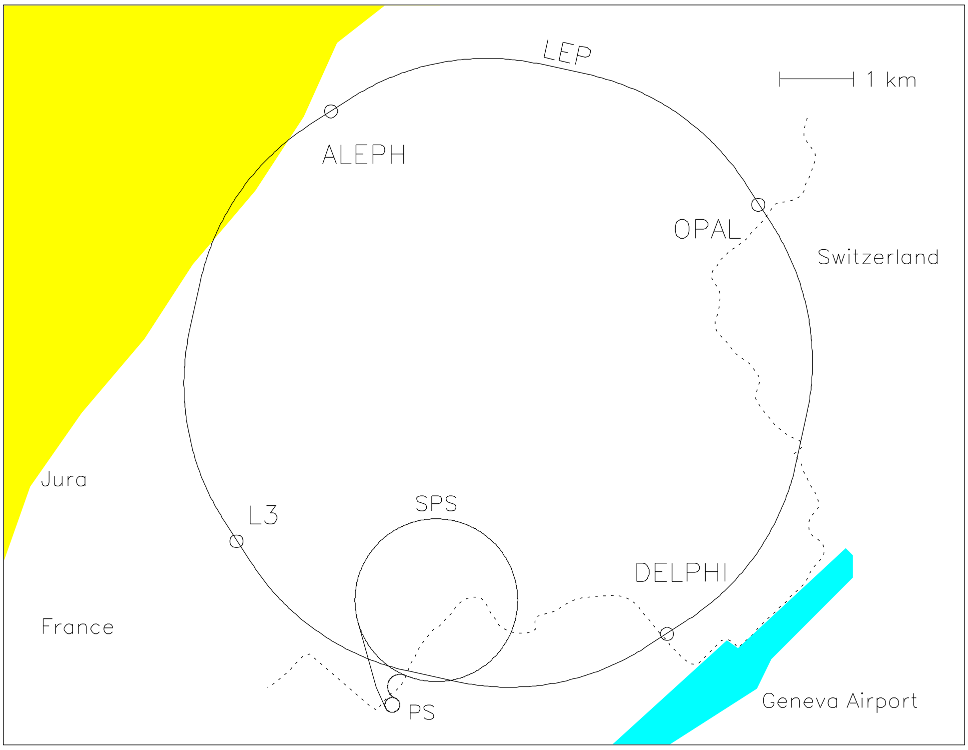

Figure 2.1 Map of the area near the LEP collider. PS, SPS and the LEP rings are shown, together with the four LEP experiments ALEPH, DELPHI, L3 and OPAL

Particle acceleration is achieved in a several step procedure as shown in Fig. 2.2. In the first step of positron generation, electrons are accelerated at the LEP Injector Linacs (LIL) to an energy of about 200 MeV. Collisions with a target of high atomic number Z lead to the production of positrons with an average energy of 10 MeV. A small fraction ($\simeq 0.001$) of the positrons are accelerated by the second stage LIL to 600 MeV. The electrons for the electron beam are produced by a 10 MeV electron gun and are injected directly into the second stage LIL. In the next step, the electrons and positrons are collected and held in the Electron Positron Accumulator (EPA) to increase the current of each beam. The Proton Synchrotron (PS) then accelerates the beams to 3.5 GeV followed by the Super Proton Synchrotron (SPS), which accelerates them to an energy of 20 GeV. Finally, the beams are injected into LEP where the particles are accelerated to about 45.6 GeV. The energy loss $\Delta U$, per revolution and per particle, due to synchrotron radiation is given by

$$\Delta U = 8.85 \cdot 10^{-5} \, \frac{E^4}{r} \cdot \frac{\mathrm{m}}{\mathrm{GeV}^3} \,, \tag{2.1}$$

where $E$ is the beam energy and $r$ the bending radius of the ring. The synchrotron radiation loss in LEP100 is not negligible, consuming about 1.2 MW of power per beam. It was the major constraint on the maximum beam energy for LEP100 with the original accelerator sections.

Each beam is concentrated in short time bunches with a length of $\approx$ 4.5 cm. The transverse

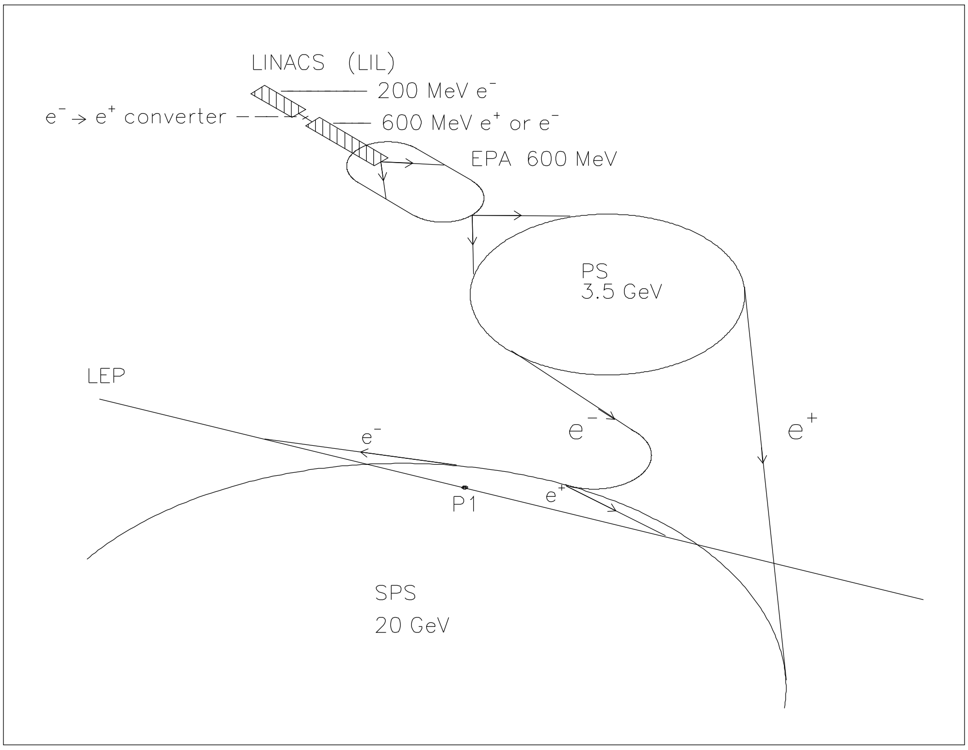

Figure 2.2 Schematic view of the LEP injection system, which shows the two stage LEP Injector Linacs (LIL), the Electron Positron Accumulator (EPA), the Proton Synchrotron (PS), the Super Proton Synchrotron (SPS) and the LEP ring itself. The 10 MeV electron gun close to the $e^- \rightarrow e^+$ converter is not shown

dimensions are $\sigma_x \approx 100\ \mu$m and $\sigma_y \approx 10\ \mu$m (corresponding to an elliptic beam profile). Each bunch contains roughly $2.5 \cdot 10^{11}$ electrons or positrons and circulates around the ring 11 250 times a second. Until mid-1992, four bunches for electrons and positrons were used. Starting in 1993 LEP also operates in an eight bunch (so-called *pretzel*) mode, and it has been tested successfully to run with *bunch trains*[1]. Both bunch systems are synchronized so that they cross each other at the four interaction points, each of which is surrounded by one of the four LEP detectors: ALEPH, DELPHI, L3 and OPAL. The rate of production of $Z^0$ events at the interaction points is increased, because the transverse size of the bunches is squeezed by strong superconducting quadrupole magnets close to the detectors.

From the physics point of view, two important machine parameters are the center of mass energy $\sqrt{s}$ and the luminosity $\mathcal{L}$. The center of mass energy $\sqrt{s}$ of an $e^+e^-$ storage ring of two beams with exactly the same energy is twice the beam energy. This is the most economical way of achieving the highest possible center of mass energy. In order to get a stable beam several effects such as betatron oscillations[2], or beam-beam interactions[3], must be considered. An additional small effect which influences the beam energy is the phase of the moon. This occurs because the surface of the earth is subject to the gravitational attraction of the moon. The surface moves under this tidal force, since the Earth's crust is not completely rigid. At the new moon and when the moon is full, the Earth's crust rises by some 25 cm in the Geneva area under the effect of these tides. This movement causes a variation of 1 mm in the circumference of LEP (for a total circumference of 26.7 km), which results in a relative beam energy variation of about 220 ppm (parts per million), or $\Delta E \approx 18.5$ MeV at the $Z^0$ resonance [15].

The luminosity $\mathcal{L}$ is defined by

$$n = \sigma \cdot \mathcal{L}\ , \tag{2.2}$$

where $n$ is the number of events per second of a given process and $\sigma$ is the corresponding cross section. The luminosity depends on some specific machine parameters and can be expressed in the following way

$$\mathcal{L} = \frac{N^+ \cdot N^- \cdot k \cdot f}{4\pi \cdot \sigma_x \cdot \sigma_y}\ , \tag{2.3}$$

where $N^\pm$ denotes the number of electrons or positrons in a bunch, $k$ is the number of bunches, $f$ is the revolution frequency and $\sigma_x$ and $\sigma_y$ are the horizontal and vertical widths of the beams at the collision point. The maximum luminosity obtained at LEP in 1994 was approximately 2.2 nb$^{-1}$s$^{-1}$.

---

[1] The running with 4 bunches, dividing each bunch into a train of several (mostly 4) bunches, is called bunch train mode.

[2] Oscillations of the beam around the ideal orbit of the machine are called betatron oscillations.

[3] Electromagnetic interactions between the beams lead to an increased betatron frequency.

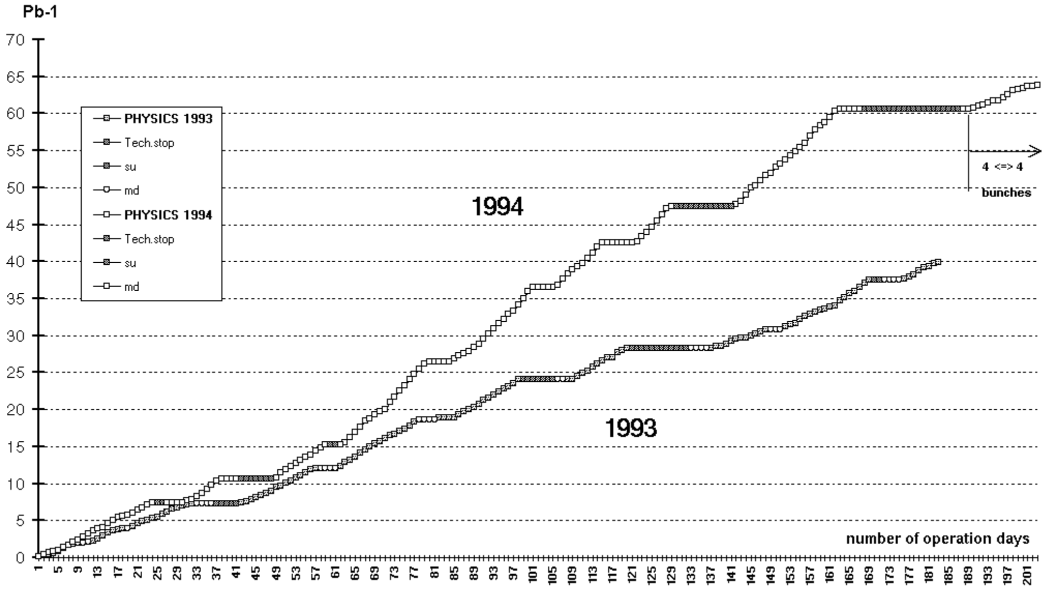

Figure 2.3 Integrated luminosity averaged over the LEP experiments in the years 1993 and 1994. The horizontal plateaus correspond to technical stops and machine developments [30]

The integrated luminosity averaged over the four LEP experiments for the years 1993 and 1994 is shown in Fig. 2.3. In summary, an integrated luminosity of roughly 270 $\mathrm{pb}^{-1}$ has been collected in the years 1990-95 by each experiment.

The beam current for an $e^+e^-$ collider is defined as

$$I^{\pm} = N^{\pm} \cdot k \cdot f \cdot e^{\pm} \ , \tag{2.4}$$

where $e^{\pm}$ is the elementary charge of the electrons and positrons. Typical beam currents for LEP during the 1994 running period were 2.5 mA.

## 2.2 The DELPHI Detector

The DELPHI detector is one of the four multi-purpose $4\pi$ detectors at LEP. DELPHI is an acronym for DEtector with Lepton, Photon and Hadron Identification. A schematic view of the apparatus is given in Figs. 2.4 and 2.5. The construction and subsequent operation is the result of a

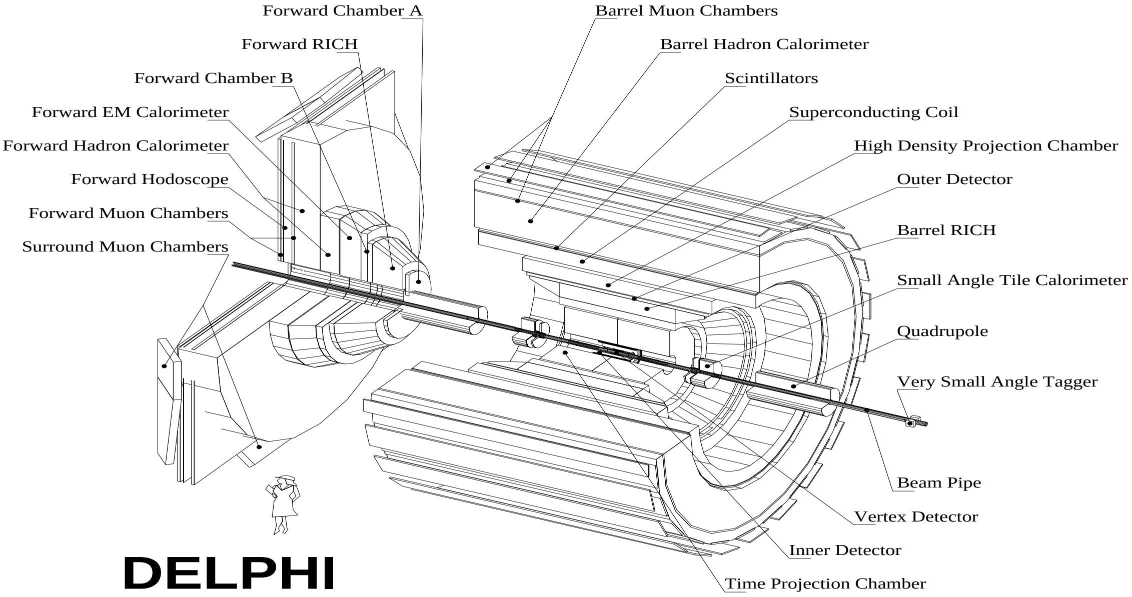

Figure 2.4 Schematic view of the DELPHI detector: Vertex Detector (VD), Inner Detector (ID), Time Projection Chamber (TPC), Ring Imaging Cherenkov Counter (RICH), Outer Detector (OD), High density Projection Chamber (HPC), Superconducting Solenoid, Time-of-Flight Scintillators (TOF), Hadron Calorimeter (HAC), Muon Chambers (MUB, MUF and MUS), Forward Drift Chambers (FCA and FCB), Small Angle Tile Calorimeter (STIC), Forward Electromagnetic Calorimeter (FEMC)

collaboration of 540 physicists from 52 different universities and national laboratories. The construction time of DELPHI was roughly 7 years. The costs for the construction of DELPHI, not including the manpower provided by the institutes, were in the order of 150 MSFr. Since the operational beginning of LEP in November 1989, DELPHI has collected over 3.5 million hadronic $Z^0$ events.

The apparatus can be divided into two regions: the cylindrical barrel-part with a total length of 8 m and a diameter of 10 m which lies axially symmetric to the beam pipe, and two large end-caps (3 m long and 10 m diameter). It has a total weight of approximately 3 500 metric tons. The detector architecture has, besides some conventional components of an $e^+e^-$ detector, additional features for particle identification, e.g. the Ring Imaging CHerenkov (RICH) detectors. The RICH was designed to achieve better separation of kaons, pions and protons over a larger momentum range than the standard methods. Most of the elements in DELPHI provide direct three-dimensional information, which is read

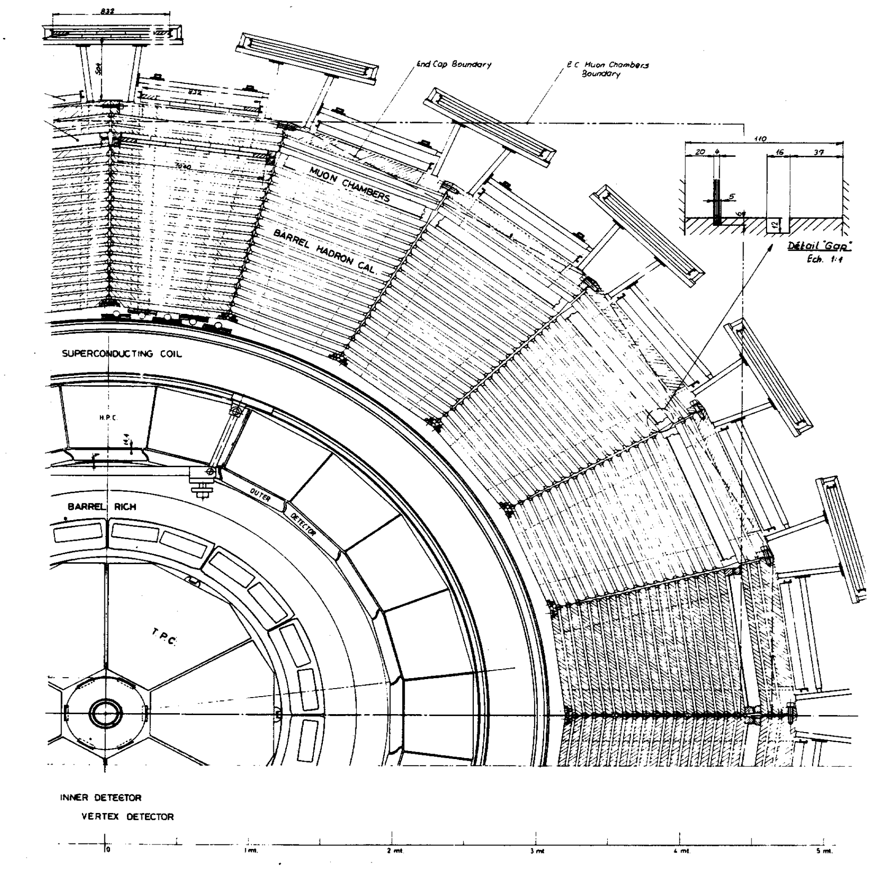

Figure 2.5 Schematic view of the DELPHI detector (barrel part) along the beam pipe

out via some 250 000 electronic channels, 14 dedicated computers and one main computer. This section reviews the main (barrel) detector components of DELPHI and provides information concerning their performance. More details can be found in Refs. [18, 33, 20, 5].

### 2.2.1 The Tracking System

#### 2.2.1.1 The Solenoid

A large part of the barrel detector is embedded in the magnetic field (1.2 T) of the large superconducting coil (length 7.2 m, inner diameter 5.2 m), made of copper-packed Ni-Ti filaments operating at $T = 4.5$ K with a total current of 5 000 A. The magnetic field allows a precise momentum determination of charged particles as a result of the measurment of curvature of the tracks in the $R\phi$ plane[4]. In addition, the magnetic field plays an essential role in reducing the transverse diffusion of the gas drift devices, e.g. in the central Time Projection Chamber (TPC) and in the High density Projection Chamber (HPC).

#### 2.2.1.2 The Vertex Detector

The DELPHI Vertex Detector (VD) consists of three layers of silicon micro-strip detectors which surround the interaction point at radii of 6.3, 9.0 and 10.9 cm parallel to the beam-pipe (see Figs. 2.6 and 2.7). Each layer consists of 24 modules covering a length of 23 cm (27 cm for the closer layer). In 1994 two layers of the VD were equipped with double-sided micro-strip detectors which provide measurements in $R\phi$ and $Z$ direction. The intrinsic resolution of the VD is 7.6 $\mu$m in $R\phi$ and 9 $\mu$m in $Z$ (for perpendicular tracks). The short lever arm to the interaction point results in a precise determination of impact parameter[5] resolution in $R\phi$ and $Z$.

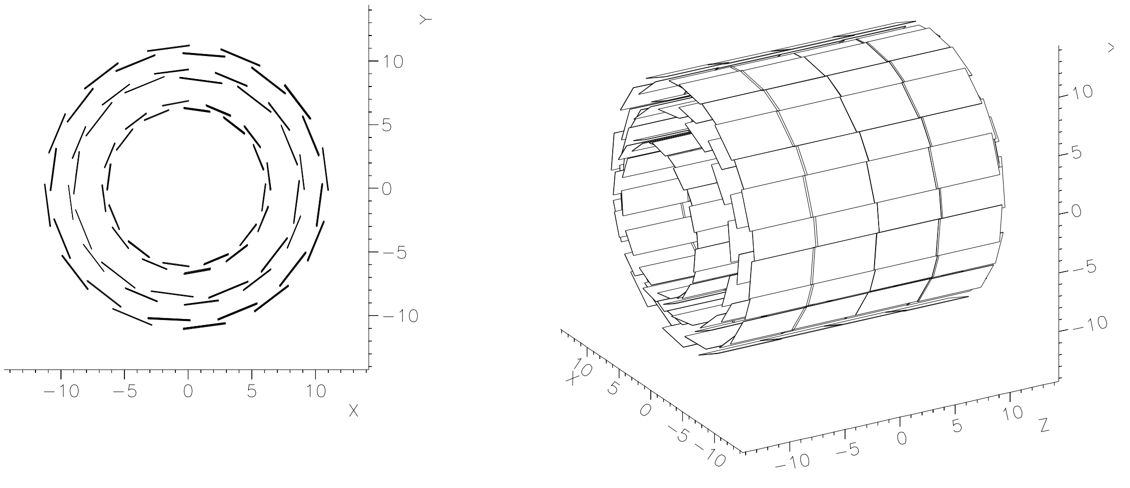

Figure 2.6 Schematic layout of the DELPHI microvertex detector (in cm). (a) Projection on the plane transverse to the beam. (b) Perspective view

The impact parameter uncertainty, $\sigma_{IP}$, has contributions from three independent sources. There is a purely geometric extrapolation uncertainty, $\sigma_0$, due to the point measurement error in the VD, the uncertainty due to multiple scattering in the beam-pipe and the layers of the VD, $\sigma_{MS}$, and the uncertainty on the position of the primary vertex, $\sigma_V$. Thus, $\sigma_{IP}^2 = \sigma_0^2 + \sigma_{MS}^2 + \sigma_V^2$. The impact

---

[4] DELPHI has a cylinder coordinate system with the $Z$ axis coinciding with the electron beam direction.

[5] The impact parameter is defined as the distance of closest approach of a track to the primary vertex.

parameter uncertainty has successfully been parametrized for the $R\phi$ direction

$$\sigma_{IP}(R\phi) = \sqrt{\left(\frac{65\ \mathrm{GeV}\mu\mathrm{m/c}}{p \cdot \sin^{3/2}\Theta}\right)^2 + (20\,\mu\mathrm{m})^2} \quad , \tag{2.5}$$

and for the $Z$ direction

$$\sigma_{IP}(Z) = \sqrt{\left(\frac{71\ \mathrm{GeV}\mu\mathrm{m/c}}{p \cdot \sin^{5/2}\Theta}\right)^2 + (34\,\mu\mathrm{m})^2} \quad , \tag{2.6}$$

where $p$ is the track momentum [GeV/c] and $\Theta$ the corresponding polar angle [20]. To achieve the extremely high precision, which is of the order of the inhomogeneities of a smooth surface, a careful alignment of each layer is necessary. Measurements on high momentum particle trajectories (e.g. $Z^0 \to \mu^+\mu^-$) as well as the overlaps between the neighboring wafers in each layer are very useful in this respect.

#### 2.2.1.3 The Inner Detector

The Inner Detector (ID) is used for fast trigger decisions and it yields some redundancy for the vertex reconstruction and track separation done by the VD. It covers a cylindrical volume between the radii 12 cm and 28 cm and has a total length of 1 m. The apparatus is split into layers - an inner drift chamber part with a jet-chamber architecture pointing to the interaction point, and an outer MWPC[6] for radii greater than 23 cm. All wires are parallel to the beam. The jet chamber is divided into 24 sectors in $\phi$ with 24 wires each. The potential of each wire is chosen so that the drift velocity rises in the same way as the drift distance (e.g., linearly with $R$). For ideal tracks stemming from the interaction point, this configuration will lead to simultaneous read-out of pulses on the wires. This allows a fast trigger decision ($3\mu$s) for tracks coming from the interaction point. Five layers of 192 field wires in the MWPC serve to resolve the left-right ambiguity of the jet-chamber, while 192 circular cathode strips (pitch = 5 mm) give $Z$ information. The resolutions obtained for $Z^0 \to \mu^+\mu^-$ events is $\sigma(R\phi) = 50$ $\mu$m and $\sigma(\phi) = 1.5$ mrad [5]. The two track separation is about 1 mm. In the 1995 shutdown the ID was replaced, extending the device to a total length of 1.40 m.

#### 2.2.1.4 The Time Projection Chamber

The Time Projection Chamber (TPC) is the main tracking device of DELPHI. It covers the active volume from $R = 35$ cm to 111 cm ($|Z| \leq 134$ cm) and is filled by an argon-methane gas mixture ($Ar/CH_4$ : 80/20%). The TPC is divided into two hemispheres of six sectors in $\phi$. It is read out at the end-caps by 16 concentric pad rows and 192 anode wires. A track passing through the gas volume

---

[6] MWPC = Multi-Wire Proportional Chamber.

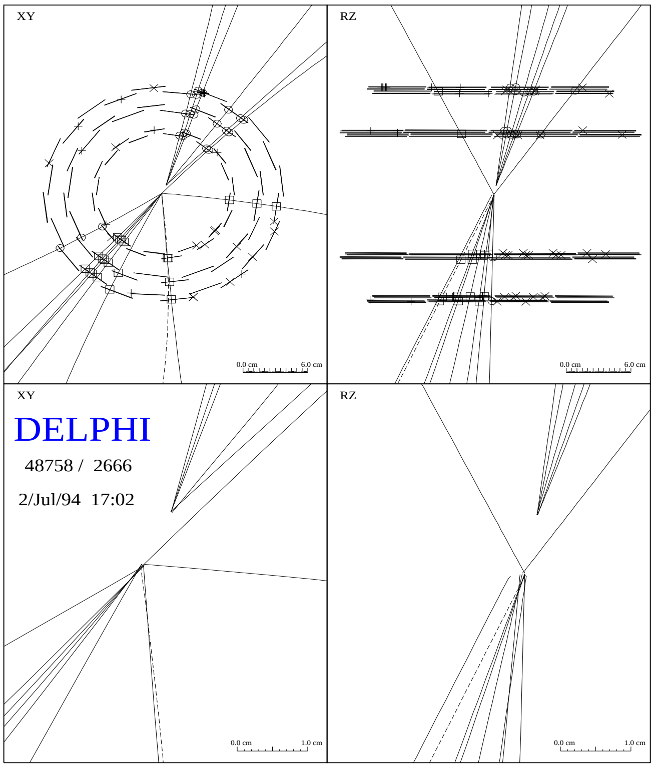

Figure 2.7 The $XY$ and the $RZ$ projection of a hadronic $Z^0$ event observed in the DELPHI vertex detector. Circles and squares indicate vertex detector hits associated to tracks, crosses correspond to unassociated hits

leaves a tube of ionization along its way. Due to a homogeneous electric field along the $Z$ direction, the charges are drifted in the gas with a drift velocity of $v_D = 6.7$ cm/$\mu$s to the end-caps. The $R\phi$ resolution is governed by the segmentation of the read-out structure, while the $Z$ coordinate is measured by the drift time. In this way, up to 16 three-dimensional space points can be measured per track. The single point resolution for tracks from multi-hadronic $Z^0$ decays is 250 $\mu$m in the $R\phi$ plane and 880 $\mu$m in the $RZ$ plane [5]. The two-point separation is on the order of 1 cm. Particle identification with the TPC is performed using the $dE/dx$ measurement for charged tracks. This is described in detail in section 3.2.

#### 2.2.1.5 The Outer Detector

The Outer Detector (OD) is a drift chamber which essentially provides fast trigger information in $R\phi$ as well as in $Z$. It consists of five layers of drift tubes at a radius between 198 and 206 cm, covering an angular region in $\Theta$ between $42^o$ and $138^o$. The OD gives points with good spatial resolution at a radius of 2 m from the interaction point, which increases the lever arm for the track reconstruction. For this reason, the OD can improve the momentum resolution for highly energetic particles. All five layers provide precise $R\phi$ measurements with a resolution of $\sigma_{R\phi} = 110\ \mu$m [5]. The longitudinal information in $Z$ is obtained by the relative timing of the signals from both ends. A resolution of $\sigma_Z = 3.5$ cm is achieved [5].

#### 2.2.1.6 The Performance of the Tracking System

The size of the central tracking devices is limited by the inclusion of the RICH detector for particle identification in the design of the DELPHI detector. Therefore, a series of several tracking components (e.g. VD, ID, TPC and OD for the barrel part) has been constructed. The alignment of the different components and the disentangling of systematic effects (e.g. shifts or torsions) is essential for a good momentum resolution. By using $Z^0 \rightarrow \mu^+\mu^-$ events the total momentum resolution in the barrel part of the detector is determined to be

$$\sigma(1/p) = 0.57 \times 10^{-3}(\mathrm{GeV/c})^{-1} \ , \tag{2.7}$$

combining VD, ID, TPC and OD track elements [5]. The momentum resolution in the forward region with $20^o \leq \Theta \leq 35^o$ is

$$\sigma(1/p) = 1.31 \times 10^{-3}(\mathrm{GeV/c})^{-1} \ , \tag{2.8}$$

using at least VD and FCB[7] information [5].

### 2.2.2 The Calorimeters

#### 2.2.2.1 The High Density Projection Chamber

The High density Projection Chamber (HPC) is the barrel electromagnetic calorimeter in DELPHI [38]. It is the first large time-projection gas calorimeter, which provides a full three-dimensional reconstruction of an electromagnetic shower. It covers the angular region $42^\circ < \Theta < 138^\circ$. The HPC consists of 144 modules arranged in 6 rings inside the cryostat of the magnet. Each ring consists of 24 modules concentrically arranged around the $Z$ axis with an inner radius of 208 cm and an outer radius of 260 cm. In principle, each HPC module is a TPC, with layers of a high density material (lead) in the gas volume, where electromagnetic showers are initiated (see Fig. 2.8). The converter thickness varies between 18 and 22 radiation lengths, depending on the polar angle $\Theta$. It consists of 40 planes of lead

---

[7] The Forward Chambers (FCA and FCB) are the main tracking devices in the forward region (see Fig. 2.4).

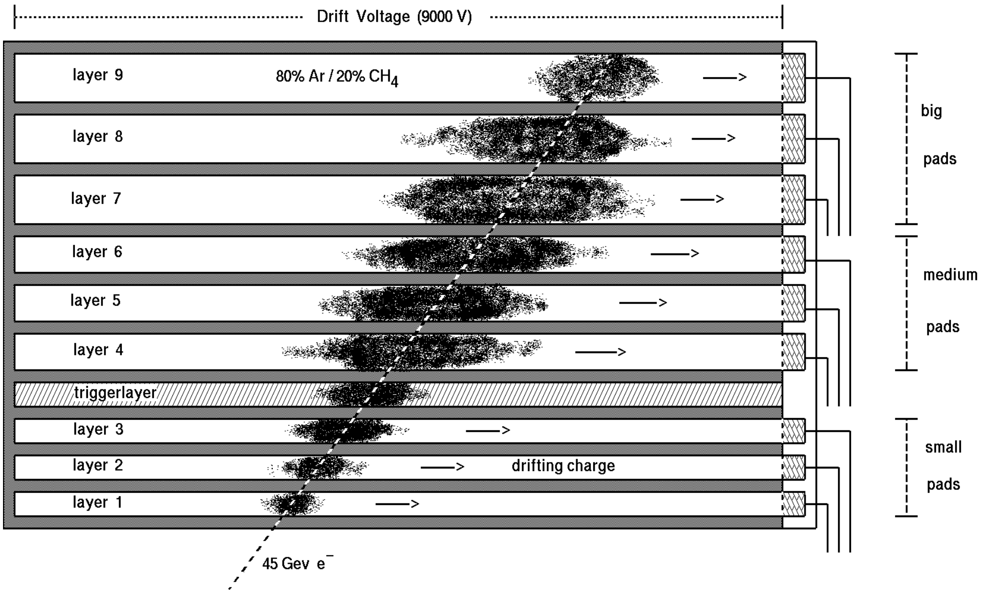

Figure 2.8 Schematic view of the layer structure of a single HPC module. An entering electron initiates an electromagnetic shower in the converter. The produced charge is drifted to a planar MWPC. The full detector consists of 144 such modules

with a thickness of about 3 mm. The 39 gas gaps are filled with an argon-methane gas mixture (Ar/CH$_4$ : 80/20%). The produced cloud of electric charge form an electromagnetic shower. It is drifted with a velocity of $v_D = 5.5$ cm/$\mu$s in a homogeneous electric field ($E = 106$ V/cm), which is parallel to the $\vec{B}$ field. The read-out of a single module is performed at the end of each module by a planar MWPC, which consists of 39 sense wires and is segmented in 128 pads. Each pad is read out in 256 time buckets. This leads to a total number of $144 \times 128 \times 256 = 4.7 \cdot 10^6$ ADC signals which are available per event. The energy resolution of the HPC for photons has been found to be[8]

$$\frac{\sigma_E}{E} = \frac{33\%}{\sqrt{E[\mathrm{GeV}]}} \oplus 4.3\% \;, \tag{2.9}$$

using neutral pions reconstructed from one photon converted before the TPC, reconstructed with high precision, and one photon reconstructed in the HPC [5]. The angular resolution in $\phi$ is given by the segmentation of the read out ($\sigma_\phi = 3.1$ mrad). The $Z$ information is evaluated from the drift time (leading to $\sigma_\Theta = 1.0$ mrad) [5].

---

[8] The $\oplus$ symbol is used to denote addition in quadrature, e.g. $a \oplus b = \sqrt{(a)^2 + (b)^2}$.

#### 2.2.2.2 The Hadron Calorimeter

The return yoke of the DELPHI superconducting solenoid is designed as an iron/gas hadron calorimeter (HAC). The angular acceptance of the instrument is $43^o < \Theta < 137^o$ in the barrel part, and $11^o < \Theta < 50^o$ and $130^o < \Theta < 169^o$ in the two forward parts. The active components of the HAC consist of 20 layers (19 in the forward region) of plastic wire chambers of 2 cm depth interleaved by 5 cm of iron. The energy resolution obtained from multi-hadronic $Z^0$ decays using the momentum information from the TPC is given by [5]

$$\frac{\sigma_E}{E} = \frac{112\%}{\sqrt{E[\mathrm{GeV}]}} \oplus 21\% \; . \tag{2.10}$$

The average depth of 1.5 m of the HAC together with the other detectors make DELPHI self-shielding so that even during runtime the detector cavern and electronics barracks are accessible.

#### 2.2.2.3 The Luminosity Monitoring Detectors

The luminosity is measured via low $Q^2$ Bhabha scatter events, which usually emerge from the interaction at small polar angles (i.e., $e^+e^- \rightarrow e^+e^-$ predominantly via photon exchange). Therefore, the Small angle TIle Calorimeter[9] (STIC) and the Very Small Angle Tagger (VSAT) are mounted 2.5 m and 7.7 m, respectively, from the interaction point close to the beam-pipe. The STIC is a lead/scintillator sampling calorimeter read out with wavelength shifting fibers and photoelectrode tubes. The VSAT is a W-Si calorimeter of 24 radiation length with the active region spanning the polar angles of 5 to 7 mrad.

### 2.2.3 Particle Identification Devices

The identification of photons, electrons, muons and hadrons is generally done in a combined offline analysis of many detector components. This section emphasizes the subdetectors which are dedicated to particle identification.

#### 2.2.3.1 The Ring Imaging Cherenkov Detectors

The aim of the Ring Imaging Cherenkov detector(RICH), shown in Fig. 2.9, is superior hadron identification over most of the momentum range by Cherenkov angle reconstruction. In each RICH detector there are two independent RICH systems; a liquid radiator and a gas radiator. The RICH detectors' principle of operation is based on their ability to detect Cherenkov radiation. Charged

---

[9] The STIC detector replaced in 1994 the Small Angle Tagger (SAT) [33].

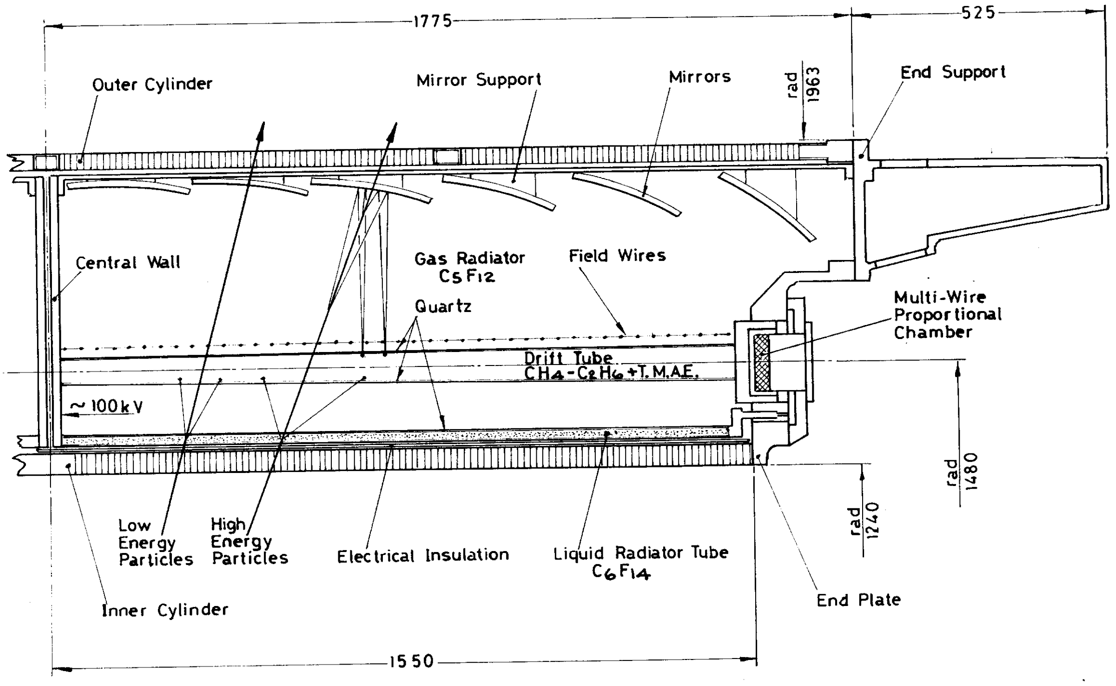

CROSS SECTION OF THE BARREL RICH

Figure 2.9 Schematic view of the barrel RICH detector. The upper volume shows the gas radiator system filled with $C_5F_{12}$. The liquid radiator volume filled with $C_6F_{14}$ is indicated as well. The Cherenkov photons are converted in $CH_4 - C_2H_6$+T.M.A.E. gas. The converted electrons drift for both systems to the proportional chamber, indicated on the right hand side. Note that the rings of the liquid and of the gas systems are displaced with respect to each other

particles traversing a dielectric medium with a velocity larger than the speed of light in that medium produce a cone of Cherenkov light. The emission angle $\Theta_{Ch}$ depends on the mass $M$ and momentum $p$ of the particle via the relation

$$\cos\Theta_{Ch} = \frac{\sqrt{1 + M^2/p^2}}{n} , \tag{2.11}$$

where $n$ is the refractive index of the radiator medium. The number of photons emitted is proportional to $\sin^2\Theta_{Ch}$. This information (Cherenkov angle and number of photons) is used to evaluate masses of charged particles. The main goal of the RICH detectors is to separate kaons and protons from the large pion background. In the momentum range where kaons and protons are below their Cherenkov threshold, they do not emit light at all, while lighter particles continue to radiate. It is this property that allows the RICH to be used in the so-called *veto mode.*

The DELPHI RICH [14] contains two radiator systems of different refractive indices. A liquid radiator is used for particle identification in the momentum range from 0.7-4.0 GeV/c, and a gaseous radiator is used from 2.5-25.0 GeV/c. The full solid angle coverage is provided by two independent detectors (the forward and the barrel RICH). Perfluorocarbons were chosen as radiator media, both in the forward (liquid $C_6F_{14}$, gaseous $C_4F_{10}$) and in the barrel (liquid $C_6F_{14}$, gaseous $C_5F_{12}$). Photons in the range from 170-220 nm are focused onto photosensitive Time Projection Chambers, 48 in number in the barrel and 24 in each arm of the forward RICH. A schematic view of the DELPHI barrel RICH is given in Fig. 2.9. More details on the operation of the RICH and the corresponding particle identification software are given in section 3.2.

#### 2.2.3.2 The Muon Chambers

The DELPHI muon chambers are drift chambers which are located behind the hadron calorimeter. The material before the muon chambers absorb most of the debris of electromagnetic and hadronic particle showers, so most hits in the chambers are due to muons. There are a total of five active planes, two in the first layer and three in the second layer, in the Barrel MUon detector (MUB). Each drift-chamber plane provides up to three signals, one anode signal and two delay line signals, which are used to give space points for particles passing through the chambers. They provide a muon identification with an efficiency of about 95%. The Barrel, Forward and Surround MUon (MUB, MUF and MUS) chambers cover the polar angular region between $15^o$ and $165^o$. Resolution measurements on isolated tracks give $\sigma_{R\phi} = 4$ mm. The $Z$ coordinate is evaluated from delay time measurements (with a digitization window of 2 ns) obtaining a resolution of $\sigma_Z = 2.5$ cm [5].

#### 2.2.3.3 The Time-of-Flight Counters

The Time-of-Flight (TOF) system is installed on the outer surface of the solenoid. It consists of a layer of 172 scintillation counters. The modules ($19 \times 2$ cm$^2$ cross section and 3.5 m long) are read out at both ends by photo-multipliers connected by light guides. In the forward part of the DELPHI detector a similar system is installed as well. In the polar angle region from $15^o$ to $165^o$ the TOF system serves as a cosmic muon trigger as well as a cosmic veto during beam crossings. Cosmic ray runs show the time resolution to be 1.2 ns [5].

## 2.3 The DELPHI Online System

The DELPHI online system has to manage several functions during runtime: analyze the events on an elementary level and supply a fast trigger decision; read out all detector components and write the data on storage media (disks, tapes); run the power supplies, gas and cooling systems of the detector and control, and log all slowly varying detector parameters (e.g. temperatures, pressures, high voltages, drift velocities, etc.).

### 2.3.1 The Slow Control System

The DELPHI slow control architecture allows a single operator to monitor and control the complete status (high and low voltages, gas supplies, etc.) of the entire detector. The performance comprises the display of the detector status, error messages and the continuous updating of the detector database for calibration and offline analysis. The 16 gas-filled subdetectors of DELPHI are supplied by a standardized gas flow control system including automatic survey of relative mixtures and the cleaning and drying of the media. This system is realized using VAXstation computers shared with the DELPHI data acquisition. The hardware link is achieved by G64-computers for the subdetectors connected by an ethernet link [9].

### 2.3.2 The Trigger

The time between two bunch crossovers is 22 $\mu$s (11 $\mu$s in 8-bunch mode). The DELPHI trigger system [22] is designed to handle large luminosities with large background event rates. The four level hierarchy starts with two hardware triggers T1 and T2. The first level decision is made within 3 $\mu$s using e.g. the charged track condition of the ID and OD or correlated wires in the FCA and FCB. Other first level trigger conditions are provided by scintillator modules mounted inside the HPC modules. If T1 fires, T2 decides within 39 $\mu$s, reanalyzing the slow drifting devices to confirm the T1 decision, e.g. the TPC for charged tracks and the HPC for electromagnetic energies. The T1 rate is usually around 400 Hz, the T2 rate around 4 Hz. T3 and T4 are software triggers running in real time. T3 confirms the T2 decision using the full granularity and resolution rejecting roughly half of the T2 events. The fourth level trigger program suppresses remaining background, flags events for physics analyses and provides an online event display for monitoring purposes [25]. There are at least 15 different trigger conditions for the levels 1 and 2 and further logical combinations are possible. The trigger system is highly redundant so that the efficiency can be tested by data itself. The efficiency for multi-hadronic events is almost 100%.

### 2.3.3 The Data Aquisition System

The heart of the DELPHI Data Aquisition System (DAS) [35] is a VAX8700 computer supported by a VAX4000 and several VAX and DEC5000 workstations. All T2 events are stored as raw data on IBM-3480 cassettes using the ZEBRA[10] bank structure. The typical size of a multi-hadronic event is 250 Kbytes in the form of raw, or unprocessed, data. The events are flagged with the *fill number* of the LEP machine and with the DELPHI *run number*. A run is defined as a period of stable conditions e.g. constant temperature, pressure, high voltages and other detector parameters. Each run is a separate file on the output tapes.

## 2.4 The DELPHI Offline Analysis Chain

This section gives an overview of the DELPHI offline analysis chain. The main components are shown in Fig. 2.10.

### 2.4.1 The DELANA Package

The main reconstruction program is the DELPHI ANAlysis program DELANA [31]. It contains one module for each subdetector which performs the necessary alignment and calibration of the raw data. The data format inside DELANA is based on ZEBRA and is called TANAGRA. The event reconstruction proceeds in the following steps:

- A local pattern recognition is performed independently and separately for each subdetector resulting in so-called Track Elements (TE's) e.g. space points and directions, energy depositions and so on. This step is known as *first stage pattern recognition.*
- The track elements from several detectors are grouped into track candidates and a first track fit is performed.
- After resolving ambiguities, the tracks are extrapolated to obtain precise estimates for their passage through the subdetectors.
- A *second stage pattern recognition* is performed, where the local pattern recognition is redone using the appropriate extrapolated information from the other subdetectors.
- Energy depositions in the calorimeter are either successfully linked to charged tracks or are marked as neutral energy.

---

[10] ZEBRA is a memory management program which offers the possibility of handling dynamic data structures.

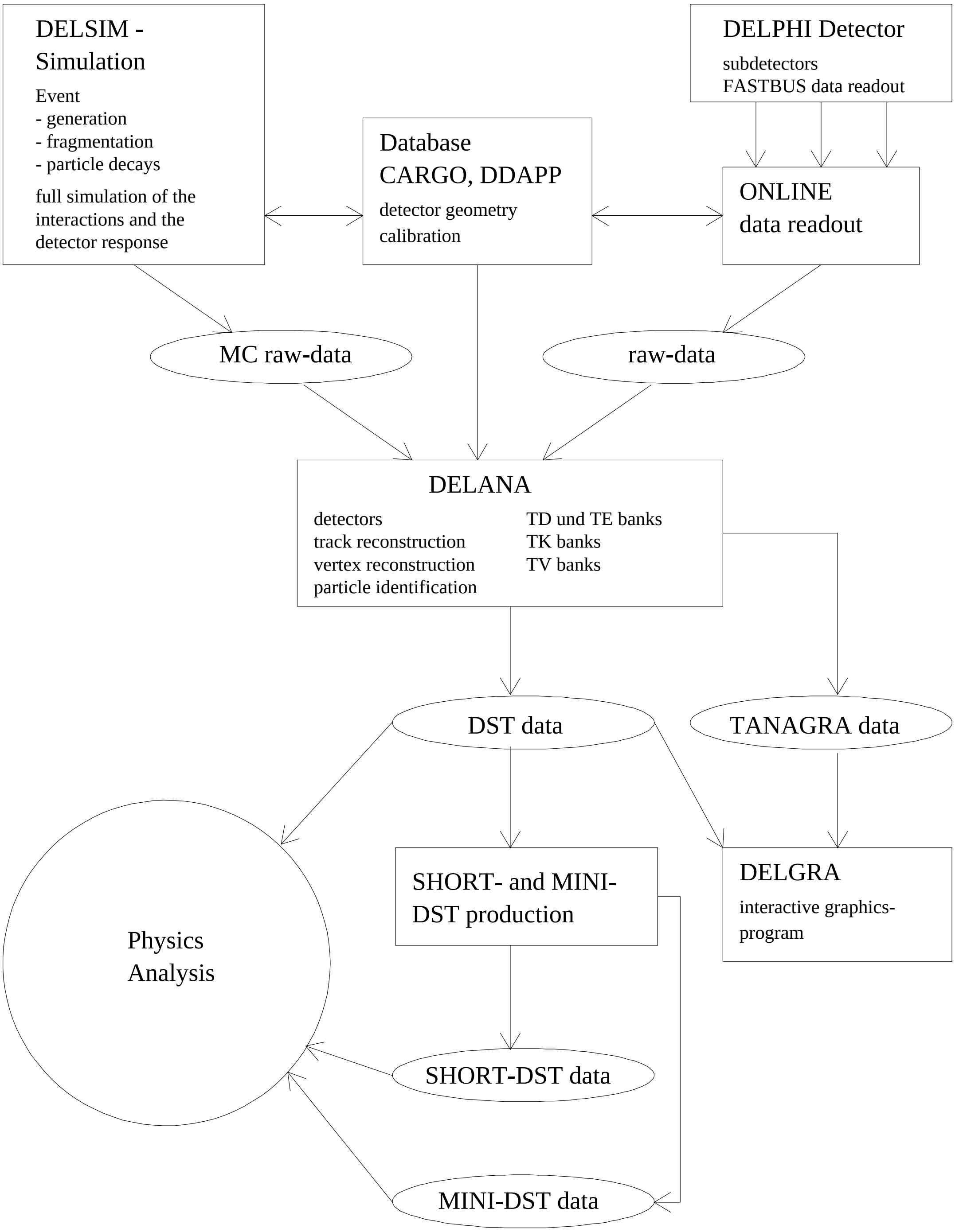

Figure 2.10 The DELPHI offline analysis chain

- Primary event vertices are fitted from the reconstructed tracks.

The output of this procedure is the so-called DST[11] data format containing a tree structure of banks based on the reconstructed vertices. All information related to physics analysis (e.g. four-vectors of particles, calorimeter information, matches to the simulation etc.) is stored here. The size of a multi-hadronic $Z^0$ DST event is roughly 65 Kbyte.

### 2.4.2 The SDST Creation

In order to improve data quality and to provide reasonable particle identification for the collaboration, an additional processing is performed. It reduces the amount of data by a factor of three and is called Short DST (SDST). It contains the following:

- Track and vertex fits are redone after fixes for alignment and calibration have been applied on the TE basis (DSTFIX).
- Running of the AABTAG package (tagging of $b\bar{b}$ events)
- Running of the MAMMOTH package (identification of interactions with detector material)
- Running of the ELEPHANT package ($e, \gamma$ and $\pi^0$ identification)
- Running of the MUFLAG package ($\mu$ identification)
- Running of the RECV0 package ($\Lambda$ and $K^0$ identification)
- Running of the HADIDENT package ($K^\pm$ and $p$ identification)

In order to reduce the volume of data by an additional factor of three (now we are down to 8 Kbytes for a typical event), a subsample of the SDST data is produced which is called Mini DST (MDST). The MDST data format contains just the basic information which is needed for an analysis, e.g. track refits are not possible using this format.

The time consuming processings (DELANA and SDST production) are done on the DELFARM computer cluster consisting of 15 ALPHA-OSF, DEC-ULTRIX and VAX-VMS workstations. The analyses presented in this thesis are based on the SDST data format. The programs analyzing the SDST data ran on the DELPHI SHIFT system consisting of seven HP-UX and four ALPHA-OSF UNIX workstations.

---

[11] DST = Data Summary Tape [42]. The DST data format is based on ZEBRA and is produced from TANAGRA data by the program package PXDST.

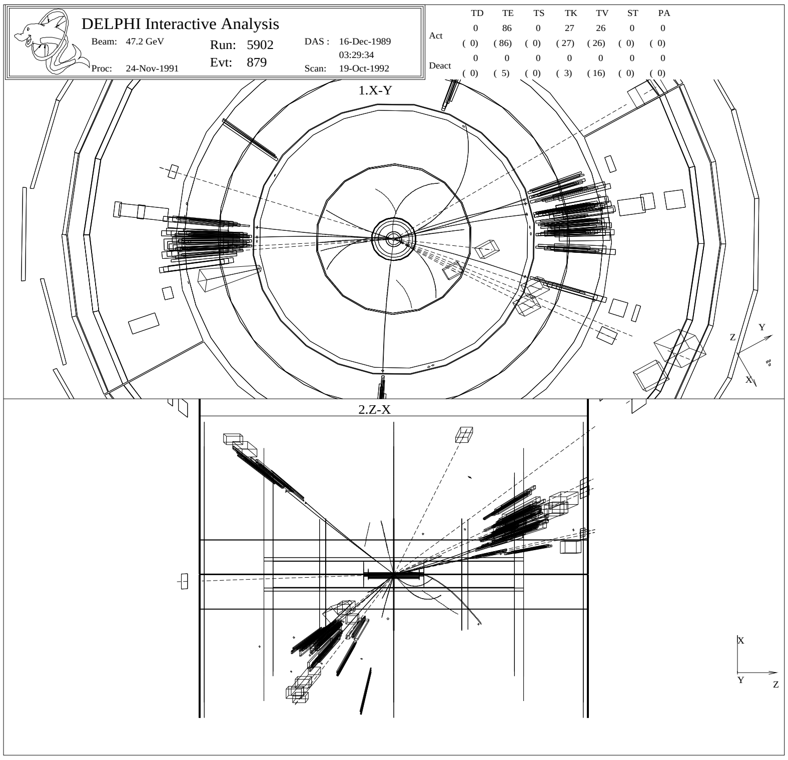

Figure 2.11 A three-jet event recorded with the DELPHI detector and visualized with the DELGRA event display program. Individual charged tracks are drawn as lines and energy depositions in the calorimeters as boxes. The upper and lower plot show the views in direction and perpendicular to the direction of the beam pipe

### 2.4.3 The DELPHI Event Display

The DELPHI GRAphics program, DELGRA, is a 3-D interactive color display facility to visualize the detector response of an event. It is very useful for investigations of the detector performance and for checks of event reconstruction programs, e.g. shower reconstructions and track fits. Especially in the LEP200 phase, where very low event rates are expected and new physics could show up, the DELGRA program will be of major importance. A set of pattern recognition routines using on-line event processing sends possibly interesting (new physics) events to the DELGRA display in the DELPHI control room. The display is updated every half-hour or so, giving the Quality Checker an opportunity to visually scan current events of possible interest. A three-jet event visualized by DELGRA is shown in Fig. 2.11.

## 2.5 The Detector Simulation

The primary aim of a simulation program is to produce "data" for a particular reaction which are as close as possible to the real raw data from the detector. These "data" are then processed through the reconstruction program DELANA and the subsequent analysis programs in exactly the same way as for real data. This procedure models the detailed response of the complete detector to a particular physics subject. The DELPHI simulation (DELSIM) [32] is based on three components which can be summarized as follows:

- Modeling the primary physics process: In most cases, this is performed by external programs, like JETSET [45] for quark final states, DYMU3 [29] for $e^+e^- \to \mu^+\mu^-$, BABAMC [19] for $e^+e^- \to e^+e^-$, KORALZ [37] for $e^+e^- \to \tau^+\tau^-$. The DELPHI collaboration uses its own parameter tuning for the different generators determined from the latest available data [23].
- Propagating the particles through the DELPHI detector including subsequent interactions with detector material, and the decay of long-lived particles such as $\Lambda$ and $K^0$. This is continued up to the point where the particles hit an active detector component: This process is modeled by stepping through the magnetic field including the possibility that these particles give rise to secondary interactions. In order to reach the required accuracy for the results, a very detailed description of the material inside the detector is necessary.
- Following the particles inside the active detector components and the simulation of the detector response as recorded in reality: This part is specific to every detector component and the modularity of the code is such that each of the detectors has a corresponding independent software module.

The particle tracking through the DELPHI detector includes energy loss, multiple scattering and the following secondary processes:

- *the photoelectric effect* - photon absorption by an atomic electron
- *the emission of Cerenkov radiation* - photons emitted by a charged particle travelling faster than the phase velocity of light in that medium
- *bremsstrahlung* - photon emission resulting from the acceleration of a charged particle in the electric field of a nucleus
- *annihilation of positrons* - conversion of mass to energy in the annihilation of an $e^+e^-$ pair

- *pair production* - conversion of an initial photon into an $e^+e^-$ pair
- *Compton scattering* - scattering of photons on free electrons, or an electron whose binding energy is negligible compared to the photon energy
- *weak decays* - decay of long-lived particles such as $\Lambda$ and $K^0$
- *nuclear interactions, using GEANTH [28]* - nuclear scattering and direct reactions resulting from the collision of a particle with a nucleus

The material parameters which determine the rates of the above processes are extracted from the CARGO data base. When a particle enters an active detector component the control of the track-following is given to the corresponding software module. Most modules follow the particles by using tools provided by the general routines outlined above. Some modules use different methods, for example the HPC which needs a very accurate description of the electromagnetic effects and is based on EGS4 [41]. When a particle crosses the sensitive volume of a detector the relevant information is stored to compute the detector response in the form of electronic signals, as for real data.

The simulation of events for physics analyses and detector studies is produced in several production centers in the DELPHI member states. The achieved statistics is comparable to or larger than the statistics for the actual LEP data. A larger sample of simulated events leads to a reduction in statistical error. This becomes important when we are looking at a rare process, or one for which there is a low efficiency, as is the case for $\Sigma^0$ reconstruction. Statistical error can be reduced at the cost of additional CPU time.

## 2.6 Summary of the Chapter

- LEP is the largest storage ring ever built. The luminosity of 2.2 nb$^{-1}$ s$^{-1}$ was reached using 8 bunches per $e^+e^-$ beam in pretzel orbits. LEP is operating on the $Z^0$ resonance with good performance close to the design values.

- DELPHI is one of the four LEP experiments. It is equipped with a large superconducting coil producing a magnetic field of 1.2 T. The electromagnetic calorimeter HPC and the RICH systems are located inside the superconducting coil which restricts the volumes of the central tracking devices.

- In the years 1990-1995 DELPHI collected an integrated luminosity of roughly 270 pb$^{-1}$. About 3.5 million hadronic $Z^0$ decays have been recorded on tape.

- The track resolution is dominated by the DELPHI vertex detector consisting of three layers of silicon microstrip diodes. The impact parameter resolution can be parametrized as $\sigma_{IP}(R\phi)[\mu\mathrm{m}] = \sqrt{\left(65/p/\sin^{3/2}\Theta\right)^2 + (20)^2}$ for $R\phi$. The corresponding resolution in the $Z$ direction is given by $\sigma_{IP}(Z)[\mu\mathrm{m}] = \sqrt{\left(71/p/\sin^{5/2}\Theta\right)^2 + (34)^2}$.

- The momentum resolution of the DELPHI tracking system was determined to be $\sigma(1/p) = 0.57 \times 10^{-3}(\mathrm{GeV/c})^{-1}$ for the barrel and $\sigma(1/p) = 1.31 \times 10^{-3}(\mathrm{GeV/c})^{-1}$ for the forward region.

- The energy resolution of the electromagnetic calorimeter HPC was found to be $\sigma_E/E = 33\%/\sqrt{E[\mathrm{GeV}]} \oplus 4.3\%$. The energy resolution of the hadron calorimeter is described by $\sigma_E/E = 112\%/\sqrt{E[\mathrm{GeV}]} \oplus 21\%$.

- Special emphasis during the construction of DELPHI was given to the particle identification devices. Good separation between kaons, protons and pions is achieved by using the barrel and forward RICH detectors. Furthermore, DELPHI is equipped with $4\pi$ muon chambers.

- The DELPHI online system manages several functions during runtime: analyze the events on an elementary level and supply a fast trigger decision; read out all detector components and write the data on storage media; run the power supplies, gas and cooling systems of the detector and control and log all slowly varying detector parameters.

- The offline analysis (DELANA, SDST production) is done on the DELFARM computer cluster, consisting of 15 DEC-ALPHA workstations. The processed data are stored for physics analysis in the DST (Data Summary Tape), SDST (Short DST) and MDST (Mini DST) format. The presented analyses were performed at CERN using the SDST format and the DELPHI SHIFT computer system.

- The simulation for physics analyses and detector studies is produced in several production centers in the DELPHI member states. The achieved statistics is comparable with LEP statistics.

# 3 ANALYSIS TOOLS

This chapter describes the main software used for the analysis. These tools are algorithms used by DELPHI members for physics analyses. They are products of various tasks within the collaboration. After the hadronic event selection is performed, the standard DELPHI algorithms for $\Lambda$ and converted $\gamma$ reconstruction are used to find the $\Sigma^0$ decay products (sections 3.2 and 4.3). As an extension to the standard $\Lambda$ reconstruction, a method of partial-reconstruction of the $\Lambda$ is implemented via proton-tagging with the RICH (section 4.2).

## 3.1 Hadronic Event Selection

The hadronic event selection in DELPHI is based on the reconstruction of charged particle tracks and neutral energy deposition in the calorimeters. Prior to the actual event selection, a track selection takes place which removes badly reconstructed tracks or tracks originating from secondary interactions with the detector material. The following track quality cuts are applied:

- track length $> 30$ cm
- track momentum $> 0.1$ GeV/c
- radius of first measured point $< 35$ cm
- $R\phi$ impact parameter $< 4$ cm
- relative error on $R\phi$ impact parameter $< 2$
- $Rz$ impact parameter $< 4$ cm

Electromagnetic showers are selected by using the default quality cuts from the ELEPHANT package [27]. Neutral showers reconstructed in the hadron calorimeter (HAC) are accepted if their energy exceeds 10 GeV. The multi-hadronic event selection comprises the following standard selection cuts (for details see Ref. [1]):

- number of charged tracks in the event $\geq 6$
- number of neutral particles in the event $\geq 1$
- $|\text{positive} - \text{negative}|$ charged particles in the event $\leq 5$
- charged energy in the event $\geq 20$ GeV
- total energy in the event $\geq 30$ GeV

After these cuts one obtains a sample of 3.16 million multi-hadronic events taken with the DELPHI detector in the years 1992-1995. The following SDST data sets are used: **92D2** - 631K, **93C1** - 706K, **94B3** - 1140K, and **95C1** - 678K. Background originating from *beam-gas* and *beam-wall* events is significantly suppressed. The contribution of these backgrounds to the event sample is estimated to be of the order of 0.1%. The background from $\tau^+\tau^-$ events is of the order of 0.2%.

The impact parameter[1] is defined as the distance of closest approach of the trajectory of a charged particle to the primary reconstructed vertex. It is evaluated separately in the $R\phi$ and $Rz$ planes. The sign of the impact parameter is defined with respect to the jet direction. It is positive if the vector joining the primary vertex and the point of closest approach to the track lies in the same direction as the jet to which the given track belongs. The sign is computed in two dimensions when only $R\phi$ measurements from the VD are available, otherwise it is done in three dimensions [2]. The sign of $R\phi$ and $Rz$ impact parameters are the same for a given track. The impact parameter error arises from the error on the point of closest approach and the error on the vertex position. The significance $S_0$ of a given track is defined as the impact parameter (in $R\phi$ or $Rz$) divided by its error. In the track selection above, only the significance in $R\phi$ is used.

## 3.2 Hadron Identification

The algorithm and performance of the DELPHI hadron identification is discussed in this section. It is based on the specific ionization measured by the TPC and the reconstructed Cherenkov angles in the RICH detectors. The portion of the analysis which depends upon particle identification (the extended $\Lambda$ finding algorithm) is restricted to the barrel region where there is complete VD, OD, TPC, and RICH detector coverage ($|\cos(\Theta)| \leq 0.788$ with $\Theta$ being the angle between the particle trajectory and the $Z$ axis).

---

[1] The impact parameter and the obtained resolutions in DELPHI are also discussed in section 2.2.1

[2] Starting from 1994 the DELPHI vertex detector provides both $R\phi$ and $Rz$ information.

### 3.2.1 Specific Ionization from the TPC

In addition to providing a three-dimensional track reconstruction, the DELPHI TPC is useful for charged particle identification by measuring the energy loss per unit length, $dE/dx$. The sense wires of its proportional chambers provide up to 192 ionization measurements per track. The signals collected by the sense wires are associated to the tracks reconstructed by the TPC pads. This association is done by comparing the time of arrival of the pad and sense wire signals. Hits too close in time to be correctly separated are not used for the $dE/dx$ calculation. This requirement corresponds, for tracks orthogonal to the drift direction $Z$, to a separation of at least 2 cm. It should be noted that an average of 5% of the signals collected by the sense wires are below the electronic threshold. The fraction of the Landau distribution lost due to this effect is a function of the drift length and gap size. To reduce this dependence, an effective threshold is applied which depends on these quantities [5].

For particle identification, the truncated $dE/dx$ is required to have at least 30 measurements. The efficiency obtained after these requirements is 61% for tracks in multi-hadronic events with momentum greater than 1 GeV/c and $|\cos\Theta_{thrust}| < 0.7$ [5]. The measured signals are corrected to take into account the usual dependence on parameters like gap size or drift length. The dependence of $dE/dx$ on the ratio $p/m$ of the track is measured from the data using various samples, and the final result can be seen in Fig. 3.1.

The resolution on $dE/dx$ estimated from data is 6.7% for pions ($p > 2$ GeV/c) coming from $K^0$ decays in multi-hadronic events, and 5% for muons ($p = 45$ GeV/c) from dimuon events ($Z^0 \rightarrow \mu^+\mu^-$) [5]. With the obtained resolution and dependence of $dE/dx$ on $p/m$, the separation between electron and pion is above 3 standard deviations for momenta below 4.5 GeV/c. A pion/heavy separation[3] can be achieved at the $1\sigma$ level above 2 GeV/c [5].

### 3.2.2 Detection of Cherenkov Radiation

The detection of Cherenkov light with the RICH detectors has already been described in section 2.2.3. In the 1994-95 data taking period 2.4 million events were recorded with a fully operational RICH detector. In previous years, the Barrel RICH recorded 0.24 million events with both radiators, and 0.73 million events with the gas radiator only. The identification power of the RICH depends on the accuracy of the Cherenkov angle measurement and on the detected number of photoelectrons. Stable operation of the different subsystems and monitoring of the relevant detector parameters is therefore very important. Table 3.1 shows averaged resolutions for both single photoelectrons and the resulting

---

[3] separation from heavy particles means pions are distinguished from kaons and protons

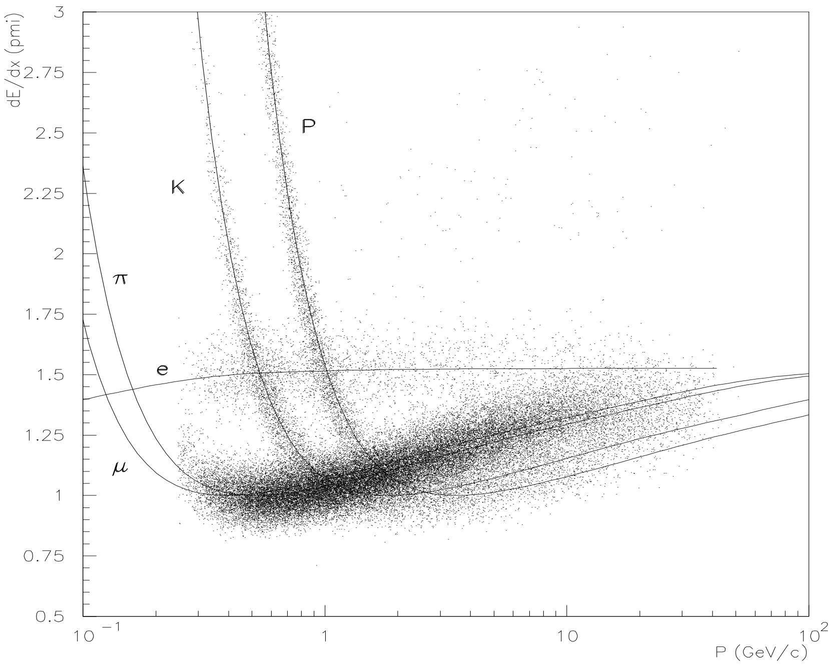

Figure 3.1 Specific energy loss, $dE/dx$, in the TPC as a function of momentum. The full lines correspond to the expectations for $e$, $\mu$, $\pi$, $K$ and $p$ tracks [5]

average Cherenkov angle per track. A detailed simulation program that takes into account all known detector effects was tuned to reproduce the data.

Several particle identification algorithms have been developed in order to fulfill very different requirements. Some physics analyses need individual track tagging, while others measure statistically the content of a given sample, without associating tags to each track. For track by track tagging, the observed signal is compared with that expected for known particle types, namely $e$, $\mu$, $\pi$, $K$ and $p$, at the measured momentum. Depending on the decay mode analyzed, the priority may be high rejection or high efficiency. The requirements also depend on the dominant source of combinatorial background: pion rejection only, or proton/kaon separation. For statistical analyses, one needs a continuous estimator of the observed Cherenkov angle, independent of any mass hypothesis, such that the number of particles of a given type can be determined.

In a hadronic event, the main difficulty is how to deal with the background under the Cherenkov signal, whose shape and level is different for each track and is a priori unknown. The algorithms

Table 3.1 Cherenkov angle reconstruction in the RICH detectors. Number of photoelectrons and angular resolutions (in mrad) for the Barrel (B) and Forward (F) RICH obtained with $Z^0 \to \mu^+\mu^-$ events [5]

| | B. liquid | B. gas | F. liquid | F. gas |
|---|---|---|---|---|
| number of photoelectrons per track | 14. | 8. | 7. | 8. |
| resolution (per photoelectron, mrad) | 13.3 | 4.3 | 11.4 | 2.5 |
| resolution (average angle, mrad) | 5.2 | 1.5 | 5.0 | 1.2 |

developed so far follow two main approaches. In the first, a flat background is fitted and no attempt is made to separate it from the signal. For each mass hypothesis, the expected signal is calculated. A flat background is adjusted in order to build and maximize a likelihood probability. The probabilities corresponding to the known particle types are then used for tagging. For statistical analyses, the likelihood probability is computed as a function of the Cherenkov angle, and the best one is retained. For further details on the HADSIGN algorithm see Ref. [26].

In the other approach, one uses a clustering algorithm to distinguish between background and signal photoelectrons. Photoelectrons are grouped into clusters, and given a weight according to quality criteria such as measurement errors or possible ambiguities between several tracks. The best cluster is retained, and weights are used to measure the average Cherenkov angle, its error and the estimated number of photoelectrons. The package which provides this information is called RIBMEAN, and further information may be found in Refs. [3, 26]. NEWTAG is an interface to the RIBMEAN weighting and clustering routine. Quality flags are set by NEWTAG to allow different rejection levels. They are based on the detector status and the cluster quality. NEWTAG also provides optimal acceptance- and momentum-windows for combined information from RICH liquid and gas radiators. The distribution of the average Cherenkov angle as a function of the momentum in multi-hadronic events is shown in Fig. 3.2 for the liquid (top) and gaseous (bottom) radiators. This can be translated into a mass measurement, as shown in Fig. 3.3. For a typical multi-hadronic momentum spectrum above 0.7 GeV/c using NEWTAG, one obtains a sample containing approximately $(46 \pm 3)\%$ kaons ($(42 \pm 3)\%$ protons) by demanding a loose kaon (proton) tag. The average efficiency for kaons (protons) is estimated to be $(52 \pm 3)\%$ ($(46 \pm 3)\%$) [43]. For further details on the NEWTAG algorithm see Ref. [43].

In both approaches outlined above, the quality of the results depends critically upon the track extrapolation through the RICH. When one requires a hit in the OD associated with the track, as is done in this analysis, smaller systematic effects (below 5% in each case) are realized.

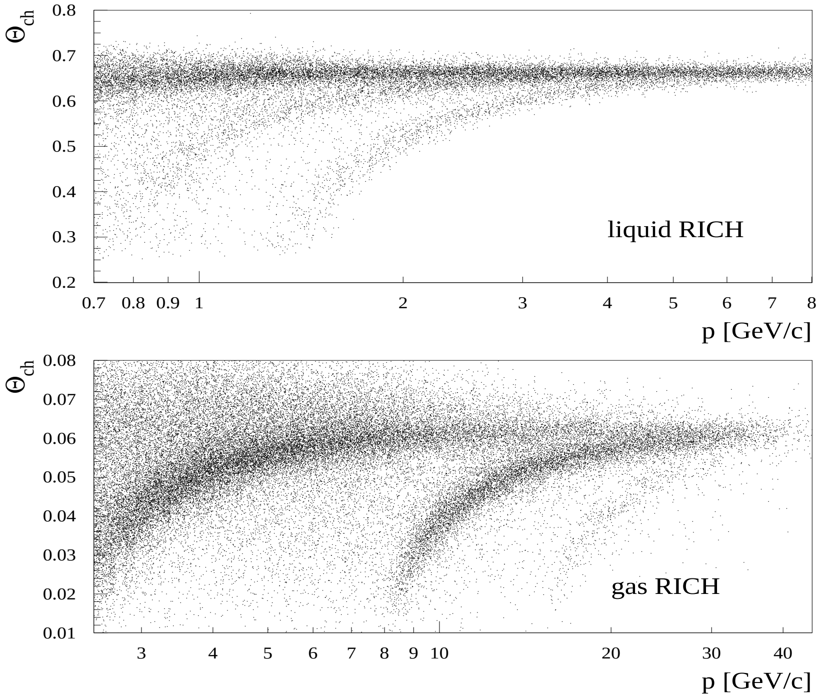

Figure 3.2 Average Cherenkov angle per track as a function of the momentum in multi-hadronic events in the Barrel RICH, for the liquid (top) and gaseous (bottom) radiators. The three bands on both plots correspond to pions (upmost band), kaons (middle) and protons (lowest band) [5]

### 3.2.3 Combination of TPC and RICH

The information originating from TPC and RICH are combined providing three different tagging levels (loose, standard and tight) for the separation of protons and kaons from pion background. Since the analysis presented is restricted to the barrel part of the detector, this discussion leaves out the performance in the forward part of DELPHI. The combined TPC-RICH algorithm discussed here is based on the DELPHI hadron identification HADSIGN. The liquid radiator is used for particle identification in the momentum range from 0.7-4.0 GeV/c, and the gaseous radiator is used from 2.5-25.0 GeV/c. Different operational modes of the RICH detector have to be considered, e.g. for the kaon tag it must be considered that the kaon band in the gas RICH starts at 8.5 GeV/c (see Fig. 3.2), which means that the gas RICH information below 8.5 GeV/c can be used *only* in the so-called veto mode. In the region

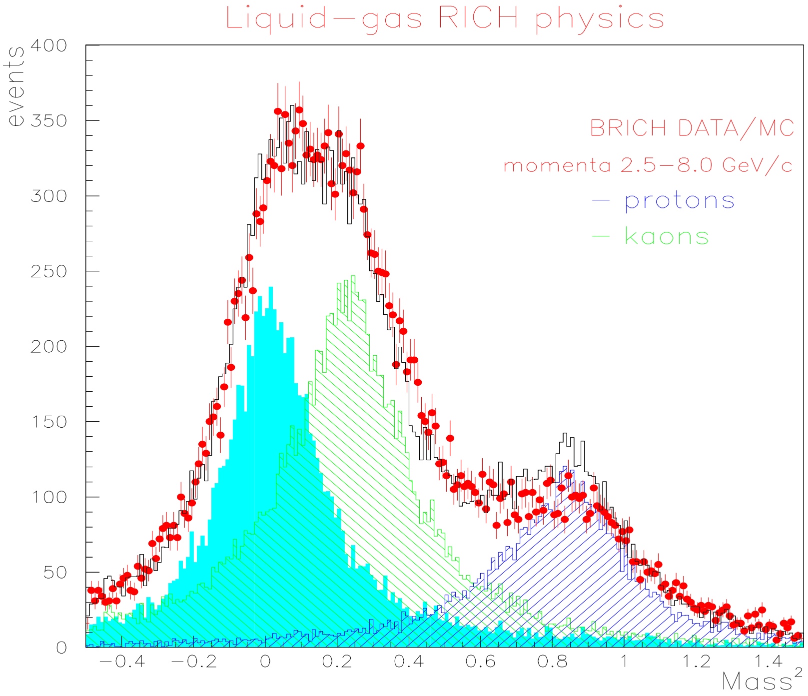

Figure 3.3 Mass derived from average cherenkov angle in the Barrel RICH, using the liquid and gas RICHes. The three shaded areas correspond to pions (solid), kaons (right-sloped hatch) and protons (left-sloped hatch). Histograms are from simulation. Data is shown as points with error bars, normalized to the same number of tracks as in simulation which pass a track quality selection

between 8.5 and 25.0 GeV/c kaons can be tagged positively from the kaon band. The performance of the tagging routines has been tested using a multi-hadronic Monte Carlo sample. The efficiency and pion rejection power for kaon tagging (loose tag - KTAG $> 0.5$, standard tag - KTAG $> 1$ and tight tag - KTAG $> 2$) as a function of track momentum is shown in Fig. 3.4a and b. Analogous data for proton tagging (loose tag - PTAG $> 0.5$, standard tag - PTAG $> 1$ and tight tag - PTAG $> 2$) are given in Fig. 3.4c and d. For a typical multi-hadronic momentum spectrum above 0.7 GeV/c and demanding a standard kaon tag (KTAG $> 1$), one obtains a sample containing approximately $(68 \pm 4)\%$ kaons. The average efficiency is estimated to be $(54 \pm 4)\%$. Similar estimations for the standard proton tag (PTAG $> 1$) lead to a sample composition containing approximately $(43 \pm 4)\%$ protons. The main background in this case originates from misidentified kaons. The average efficiency is estimated to be $(60 \pm 4)\%$. These quantities have been extracted from simulation, and verified in conjunction with the $V^0$ package

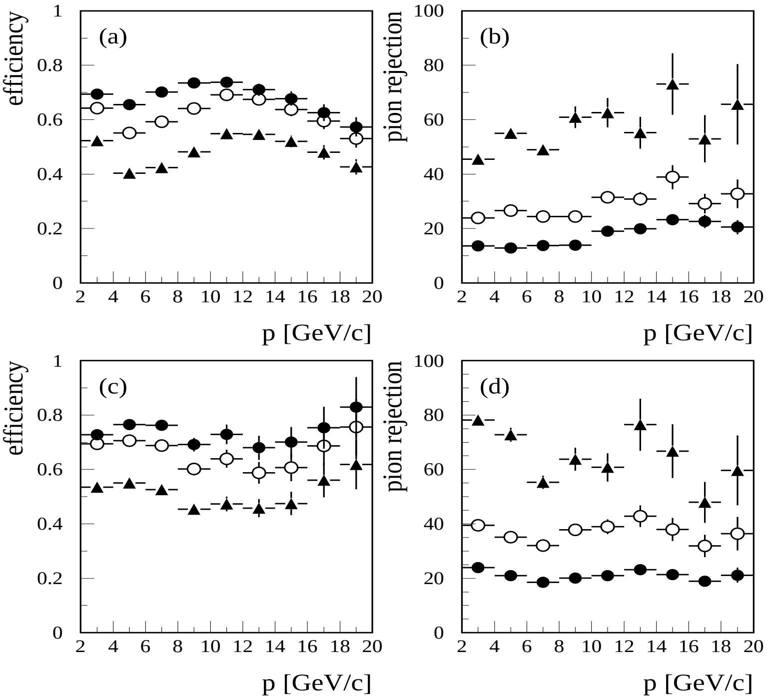

Figure 3.4 Performance of the DELPHI hadron identification (HADSIGN) in multi-hadronic events. (a) Efficiency and (b) pion rejection power for the three different kaon tags as a function of momentum (full circles - loose tag, open circles - standard tag, triangles - tight tag). (c) Efficiency and (d) pion rejection power for proton identification

as a way to identify particles in data. Systematic studies comparing data and simulation show the misidentification probability for kaon identification in Monte Carlo to be approximately a factor of two lower than in data [26].

## 3.3 $\mathbf{V^0}$ Reconstruction

This section describes the standard DELPHI algorithm for $\Lambda$ and $K^0$ reconstruction [5]. Candidate $V^0$ decays in the sample of hadronic events are found by considering all pairs of oppositely charged particles. The vertex defined by each pair is determined such that the $\chi^2$ obtained from the distances of the vertex to the extrapolated tracks (considered as ellipsoids in 5D space of perigee parameters [4]) is minimized.

---

[4] A charged particle track can be described as a helix defined by five parameters ($\Theta, \phi, \kappa, \varepsilon$ and $Z$). These parameters evaluated at the point of closest approach to the primary vertex are called perigee parameters.

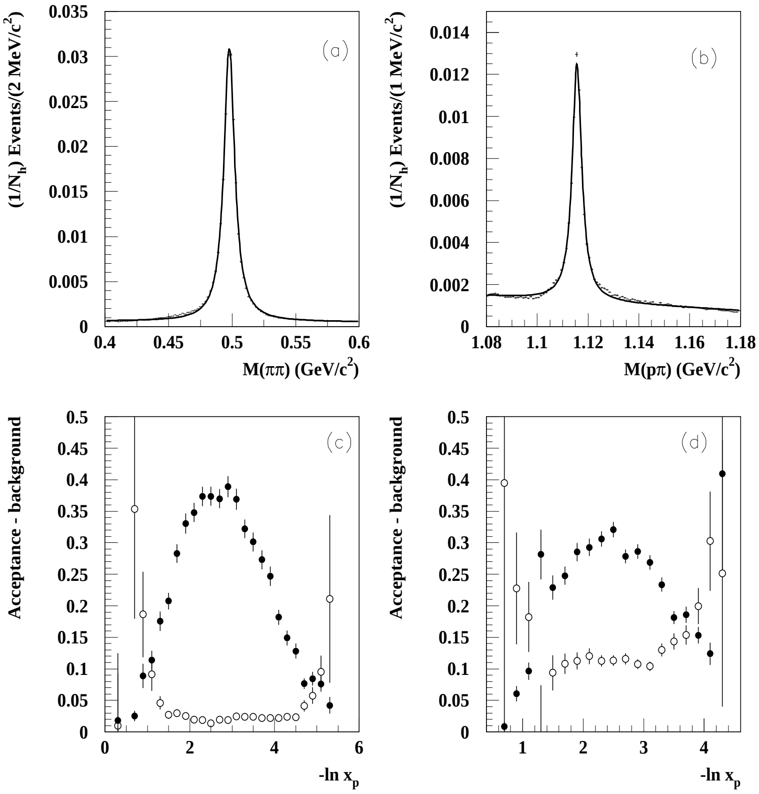

Figure 3.5 Performance of the DELPHI $V^0$ Identification. Invariant mass distribution for the tight (a) $K^0$ and (b) $\Lambda$ samples, normalized to the total number of hadronic events; the line shows a fit to a Breit-Wigner shape for the mass plus a linear background. Efficiency (closed circles) and background fraction (open circles) as a function of $\ln(x_p)$ = -$\ln(p/p_{beam})$ for tight (c) $K^0$ and (d) $\Lambda$ samples

The tight $V^0$ [5] decay vertex candidates are required to satisfy the following criteria [5]:

- The angle $\Delta\phi$ in the $XY$ plane between the $\mathrm{V}^0$ momentum and the line joining the primary to the secondary vertex is more than $(0.01+0.02/p_t)$ rad, where $p_t$ [GeV/c] is the transverse momentum of the $\mathrm{V}^0$ candidate relative to the beam axis.
- The radial separation $R$ of the primary and secondary vertex in the $XY$ plane is greater than 4 standard deviations.
- The probability of the $\chi^2$ fit to the secondary vertex is larger than 0.01.

---

[5] The sample has strict topological and invariant mass requirements which yield high purity with low efficiency

- The transverse momentum of each particle of the $V^0$ with respect to the line of flight is greater than 0.02 GeV/c and the invariant mass for the $e^+e^-$ hypothesis is less than 0.16 GeV/c$^2$.
- When the reconstructed decay point of the $V^0$ is beyond the VD radius, there is no signal in the VD consistent with association to the decay vertex.

The $\pi^+\pi^-$ and $p\pi^-$ ($\bar{p}\pi^+$) invariant masses (attributing the proton mass to the particle of larger momentum) are calculated. When a pair is consistent within three standard deviations with both $K^0$ and $\Lambda$ hypotheses, the pair with the smaller mass pull (the absolute value of mass shift with respect to the nominal mass divided by the overall resolution) is selected. Finally, $K^0$ and $\Lambda$ candidates are selected if two additional requirements are met:

- the probability to have decayed within the fitted distance lies between 0.02 and 0.95
- the difference between the invariant mass and the nominal mass is within two standard deviations.

The mean resolution, defined as the FWHM of the fitted distributions, is 4.3 MeV/c$^2$ for $K^0$'s and 1.8 MeV/c$^2$ for $\Lambda$'s from the *94B* data sample. The efficiency is strongly dependent on the V$^0$ momentum. For $\Lambda$'s the efficiency rises from 10% at 0.5 GeV/c to 32% at 3.6 GeV/c and then drops to 6% at 17 GeV/c. For $K^0$'s the efficiency rises from 9% at 0.5 GeV/c to 38% at 3.6 GeV/c and then drops to 10% at 17 GeV/c [5]. The efficiency for K$^0 \rightarrow \pi^+\pi^-$ in this selection averaged over the momentum spectrum is about 36% with a contamination of 3%. The average efficiency for $\Lambda \rightarrow p\pi$ is 30% with a contamination of about 10% [5]. The performance of the V$^0$ task's $\Lambda$ and $K^0$ identification is shown in Fig. 3.5.

## 3.4 Summary of the Chapter

- The presented analysis starts with a sample of 3 155 K multi-hadronic events taken with the DELPHI detector at LEP in the years 1992-1995. The multi-hadronic event selection is based on the reconstruction of charged particle tracks and neutral energy depositions in the calorimeters.
- The DELPHI hadron identification is based on the $dE/dx$ measurement of the TPC and the Cherenkov angle reconstruction of liquid and gas RICH. Two RICH algorithms are in use, HADSIGN and NEWTAG. HADSIGN combines RICH and TPC information, while NEWTAG is RICH-only.
- For a typical multi-hadronic momentum spectrum above 0.7 GeV/c using HADSIGN, one obtains a sample containing approximately $(68 \pm 4)$% kaons ($(43 \pm 4)$% protons) by demanding a standard

kaon (proton) tag. The average efficiency for kaons (protons) is estimated to be (54 ± 4)% ((60 ± 4)%).

- For a typical multi-hadronic momentum spectrum above 0.7 GeV/c using NEWTAG, one obtains a sample containing approximately (46±3)% kaons ((42±3)% protons) by demanding a loose kaon (proton) tag. The average efficiency for kaons (protons) is estimated to be (52 ± 3)% ((46 ± 3)%) [43].
- The DELPHI $V^0$ search algorithm is used to find $\Lambda$ and $K^0$ decays. This provides a way to tag pions and protons in data, and is used to check the performance of the DELPHI hadron identification routines. The efficiency for $K^0 \rightarrow \pi^+\pi^-$ averaged over the momentum spectrum is about 36% with a contamination of 3%. The average efficiency for $\Lambda \rightarrow p\pi$ is 30% with a contamination of about 10% [5].

# 4 THE ANALYSIS

This chapter describes a measurement of the production of the strange baryon $\Sigma^0$ in $Z^0$ hadronic decays with the DELPHI detector at LEP. A total of 3.155 million hadronic $Z^0$ decays collected during 1992-95 have been analyzed. The $\Sigma^0$ hyperon is identified through the electromagnetic decay $\Sigma^0 \to \Lambda\gamma$ (branching ratio $\sim$ 100%). The $\Lambda$ is identified through its decay $\Lambda \to p\pi^-$ ($\sim$ 64%), while the $\gamma$ is found only if it converts in the detector, $\gamma \to e^+e^-$. $\Lambda$ candidates are identified using either the standard DELPHI $V^0$ search algorithm as described in section 3.3, or using the unique capability of the RICH detector to tag proton tracks in an extended $\Lambda$–finding algorithm developed for this analysis. The efficiencies and performance of the various methods will be summarized in section 4.5.

## 4.1 The $V^0$ Algorithm to Find $\Lambda$ Candidates

The standard DELPHI $V^0$ algorithm, RECV0, is run first, accepting $\Lambda$ candidates and rejecting $K^0$ decays. This algorithm has been used in many analyses. An example from an event containing both a $\Lambda$ and a $\overline{\Lambda}$, shown in Fig. 4.1, illustrates the operation of the inner tracking system for two $\Lambda$ 's which have been fully reconstructed. The $\Lambda$ and $\overline{\Lambda}$ are shown as dashed lines. Although there were no TE's (track elements) reconstructed in the ID for the $\Lambda$ that decayed in the ID (at R = 17.9 cm), the vertex is reconstructed right in front of the first measured ID TD [1]. The tracks belonging to the $\overline{\Lambda}$ decaying at R = 4.4 cm both have three associated VD $R\phi$ hits. The figure also shows that the leading track (proton) carries most of the momentum of the $\Lambda$ . This allows for partial reconstruction of the $\Lambda$ when the pion track is either missing or poorly reconstructed, a method described in the next section. The description of the tight $\Lambda$ selection is given in section 3.3. The estimated systematic error on this procedure is $\sim$5%.

---

[1] TD's are single-point measurements that are not directly included in the track reconstruction, but only via TE's

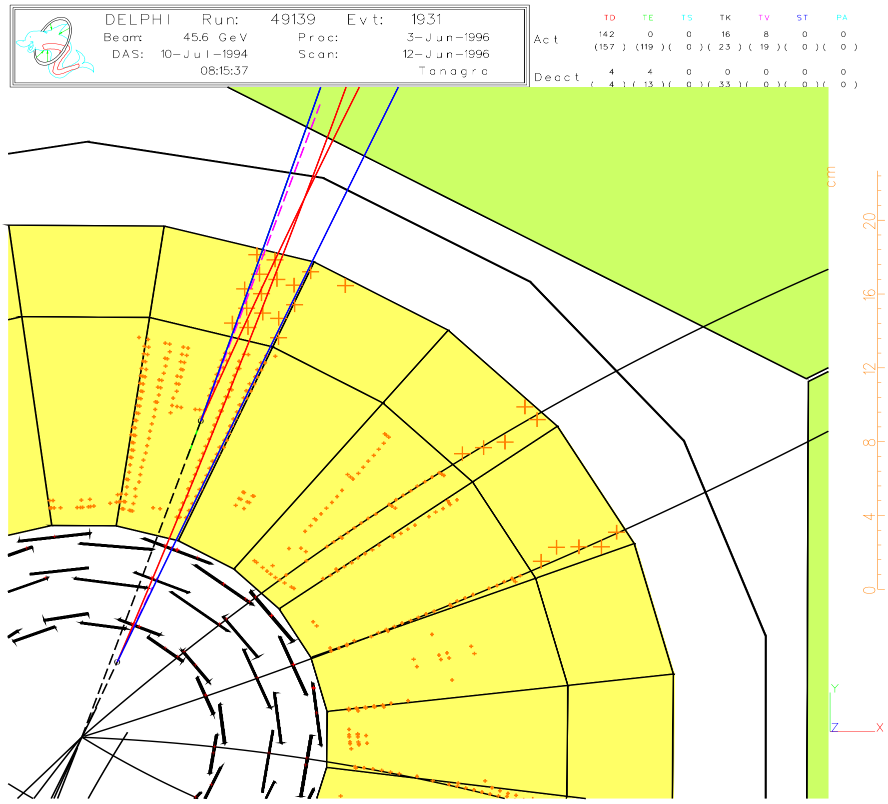

Figure 4.1 DELGRA $q\bar{q}$ event with $\Lambda$ and $\overline{\Lambda}$ decays at 17.9 cm and 4.4 cm

## 4.2 Extended Method for $\Lambda$ Recovery

The $\Lambda$-finding algorithm was extended in this analysis to include those $\Lambda$ decays where the $V^0$ was poorly reconstructed. This can occur for a variety of reasons. The inefficiency in the $V^0$ algorithm is the result of very strict cuts on the two-track hypothesis in order to reduce combinatoric background. In addition, the $\Lambda$ is relatively long-lived, and often decays in the TPC, in which case one or both of the tracks may be poorly measured. Tracks are also lost in the cracks of the active TPC volume.

Table 4.1 lists the $\Lambda$ decay categories and fraction of $\Lambda$ decays occurring for each type. The extended method was developed as an attempt to recover the $\sim 27\%$ of $\Lambda$ decays, shown in bold, that would otherwise be lost in a detector without the powerful particle identification capability of the DELPHI RICH detectors. In DELPHI, $\sim$5% of the $\Lambda$ decays are beyond the tracking volume. Other unseen decays include $\Lambda \to n\pi^0$ ($\sim 36\%$), and $\Lambda \to p\pi^-$ where both tracks are lost ($\sim 8\%$). For $\Lambda$ decays where only one track is reconstructed, the charged $\pi$ is lost in $\sim$11% and the $p$ is lost in $\sim$7%

of the total $\Lambda$ sample. We are left with $\sim$34% of the total $\Lambda$ sample where two charged tracks are fully reconstructed. The standard DELPHI $V^0$ algorithm finds $\sim$50% of those decays, or $\sim$16% of the total. The remaining $\sim$16%, and the $\sim$11% where only the $p$ track is found, are amenable to recovery via identification of a proton track detached from the primary vertex.

For the measurement performed in the first momentum bin of the $\Sigma^0$ $(0.044 < x_p < 0.100)$[2], only the standard DELPHI $V^0$ algorithm is used. The two high momentum bins make use of the extended method described here. For $x_p > 0.100$, the direction of the $\Lambda$ is well-described by the vector joining the primary vertex with the FMH (first measured hit) of the proton track. This is the direction used for the $\Lambda$ candidate in the extended method. The numbers given in Table 4.1 are averages for the entire momentum spectrum. For the sample of $\Sigma^0$ with $x_p > 0.100$, the $\pi$ track is lost $\sim$7% of the time, and RECV0 fails at a rate of $\sim$18%

Table 4.1 $\Lambda$ decay categories, with the sample amenable to recovery by the extended method shown in bold type

| Category of $\Lambda$ decay | fraction occurring, in % |
|---|---|
| beyond tracking volume | 5 |
| $\Lambda \to n\pi^0$ | 36 |
| $\Lambda \to p\pi^-$, both tracks lost | 8 |
| **one charged track lost - $\pi$** | **11** |
| one charged track lost - $p$ | 7 |
| reconstructed by RECV0 | 16 |
| **both tracks present, but missed by RECV0** | **16** |

As mentioned previously, it is possible to identify the proton track with the DELPHI detector. However, it is not enough to simply identify proton tracks, as there are plenty of protons which do not originate from $\Lambda$ decays. These would simply raise the background level in the reconstruction of the $\Sigma^0$ and reduce the quality of the measurement. To distinguish protons originating from $\Lambda$ decay from other sources of protons, we require that the reconstructed track does not have an associated VD hit. The $\Lambda$ is the only particle capable of producing a proton beyond the VD, with the possible exception of hadronic interactions with detector material and a few baryon decays such as the $\Omega^-$, all of which are short-lived compared to the $\Lambda$ . For $\Lambda$ with momentum above 3 GeV/$c$, 75% decay beyond the VD. For these reasons, an associated hit in the VD is a useful discriminator for separating protons in $\Lambda$ decays from other protons, while maintaining high efficiency for the $\Lambda$ protons. Background is further reduced

---

[2] the momentum, when expressed as fractional beam momentum, is denoted by $x_p$. It is defined as $x_p = \frac{p}{p_{beam}}$

by removing certain tracks from consideration based on previous reconstruction of $\Lambda$, $K^0$ and $\gamma$ decays, and by finding hadronic interactions. Hadronic interactions with detector material are found using the standard DELPHI software package called MAMMOTH [34].

The extended method for finding $\Lambda$ candidates finds detached proton tracks using the following criteria:

- No associated VD hit
- Required to have an associated OD hit
- Positive proton identification (described below)

To identify the charged track as a proton, the HADSIGN and NEWTAG algorithms are used. When HADSIGN identifies a standard proton using the combined information from the TPC and/or RICH detectors (XPR $\geq 2$), an oppositely charged track (the $\pi$) is required whose FMH is near the FMH of the proton candidate. The requirements for the difference in FMH for the two tracks are as follows:

- The opening angle of the vectors joining the primary vertex with the FMH of the two tracks must be less than 10 degrees
- The difference in FMH of the two tracks must be less than 10 cm in the $r\phi$ plane

When NEWTAG identifies a loose proton (IPR $\geq 1$ and JPR $\geq 0$), no additional constraints are used, as the NEWTAG algorithm has much more stringent criteria on proton identification.

The efficiency of the extended method for finding $\Lambda$ was not taken directly from simulation. Since simulation has a 100% operational RICH detector, for example, care must be taken to monitor the actual performance of the detector in data and correct for partial operation and other discrepancies. The efficiency of the extended method was corrected in data using the overlap with the standard method of the previous section. For the correction, the criteria for selecting $\Lambda$ protons was applied to the leading particle from the $\Lambda$ candidates found by RECV0 in simulation and data. This provides a large proton-enriched sample in data, which is essential for comparison. It allows the best check and correction to the proton tagging efficiency in data for the particular selection criteria we have in place. After normalization to the number of $\Lambda$ 's selected by RECV0 and the number of leading tracks passing a quality selection for particle identification, data and MC are in good agreement for both tagging algorithms used (HADSIGN and NEWTAG).

Systematic errors are estimated by varying the tagging level of particle identification. The tagging levels are assigned by a decision based on significance of the measured parameters involved. NEWTAG is recognized as having systematic errors below 5%, while HADSIGN is estimated to be less favorable. However, requiring that the track have an OD hit improves the stability of the results, and the systematics for HADSIGN drop accordingly. Systematics are estimated to be ~5% for the standard and ~7% for the extended $\Lambda$-finding algorithms. The combination of standard and extended methods yields an estimate of ~7% systematic error.

## 4.3 Converted $\gamma$ Reconstruction

The energy spectrum for the photons from $\Sigma^0 \to \Lambda\gamma$ decays peaks at about 150 MeV in the lab frame, which is not a favorable region for reconstruction in the electromagnetic calorimeter. Therefore, the photon selection in this analysis is restricted to those photons which have converted to $e^+e^-$ pairs in material before the TPC. The standard DELPHI converted photon reconstruction is used, and is detailed in this section.

Photon conversions in front of the TPC are reconstructed by an algorithm that examines charged tracks reconstructed in the TPC. Each TPC track is examined for a point P, where the tangent to the helix (in the $R\phi$ projection i.e. in the plane perpendicular to the beam) points directly to the main vertex defined by the beam spot position. Under the assumption that the opening angle of the electron-positron pair is zero, this procedure gives the conversion radius R, i.e. the transverse distance from the main vertex to the point P. In the following, all tracks which have a solution R with $R/\sigma(R) > 1$ are accepted as conversion candidates. Since the curvature decreases with increasing energy, highly energetic tracks are often compatible with both the main vertex and a secondary vertex. The one standard deviation cut is necessary to keep background at a tolerable level, but it limits the efficiency at high energies.

If two oppositely–charged conversion candidates are found with compatible decay point parameters, they are accepted as a converted photon. The following selection criteria are imposed:

- The weighted mean conversion radius of both tracks is at least one standard deviation away from the main vertex (defined by the beam spot).
- The reconstructed mean conversion radius is at least 5 cm and below 50 cm (before the main TPC gas volume).
- At least one of the tracks has no associated point before the reconstructed mean conversion radius.
- The difference in azimuthal angle $\Delta\phi$ of both conversion points is below 30 mrad.

- The difference in polar angle $\Delta\theta$ of the two tracks is below 15 mrad.

If these criteria are fulfilled, a $\chi^2$ is calculated from $\Delta\phi$, $\Delta\theta$ and the difference of the reconstructed conversion radii $\Delta R$ in order to find the best combinations in cases where there are ambiguous associations. The energy of the conversion electrons is corrected for radiation losses by a factor that depends on the amount of material between the conversion point and the entrance to the TPC. The reconstructed corrected photons with an acceptable $\chi^2$ have a precision on their energy of $\pm 1.2\%$, an angular resolution of $\pm 1.5$ mrad in $\theta$ and $\phi$, and a precision on the conversion radius of $\pm 5$ mm. These values have been obtained from simulation.

In some conversions, only one of the tracks is fully reconstructed in the TPC. These single tracks are accepted as conversions only if the following conditions are fulfilled:

- The conversion radius is between 22 and 33 cm.
- In the $R\phi$ plane the distance of the conversion radius from the main vertex is at least 4 standard deviations ($R/\sigma(R) > 4$).
- No hits are associated in front of the reconstructed conversion point.
- The z-coordinate of the conversion point and that from the angular extrapolation from the reconstructed primary vertex towards the conversion point coincide to within 1 cm.
- The reconstructed photon energy divided by $\sin\theta$ is below 5 GeV ($E_\gamma/\sin\theta < 5$ GeV).

From the simulation a precision on the photon energy of $\pm 12\%$ is obtained after applying a mean energy correction for the unseen lepton and an angular precision of $\pm 1.5$ mrad in $\theta$ and $\phi$.

Reasonable agreement between data and simulation is observed in the distribution of the reconstructed conversion radii, as shown in Fig. 4.2. However, some discrepancies are found around $R = 30$ cm, due to differences in actual detector material distribution from that used in simulation. The energy spectra of converted photons for simulated and real data are shown in Fig. 4.3.

The converted photon reconstruction is also used for an analysis of the inclusive $\pi^0$ cross section [7]. Photon energy and $\gamma\gamma$ invariant mass spectra using conversion pairs have been checked to be in general agreement with the simulation prediction. The systematic error has been evaluated at $\sim 5\%$, arising from differences in reconstruction efficiency and material distribution [7].

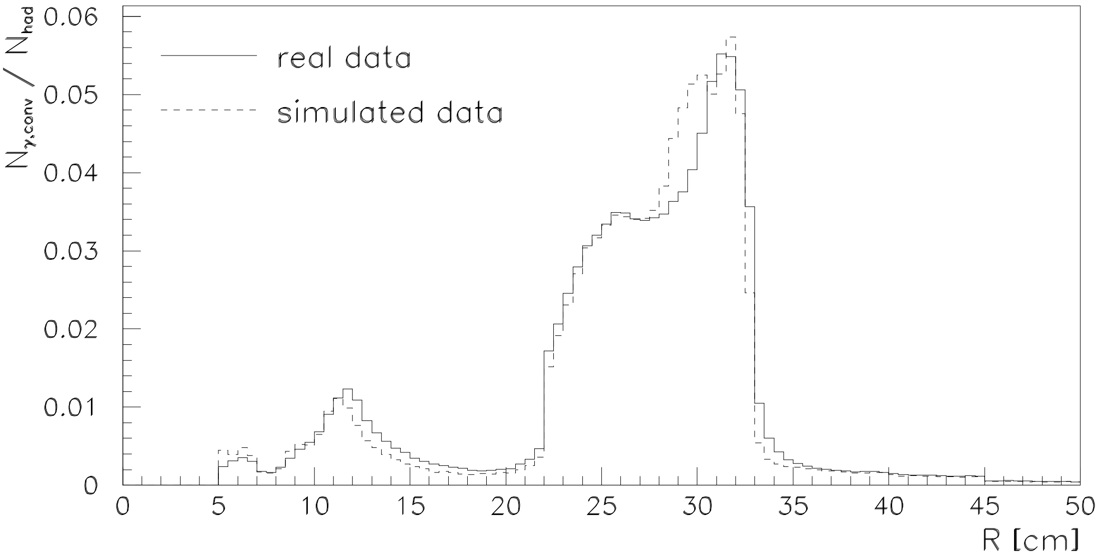

Figure 4.2 Distribution of $\gamma$ conversion radii reconstructed in the TPC for real and simulated data. The number of conversions is normalized to the number of events [7]

## 4.4 $\Sigma^0$ Selection

The $\Sigma^0$ is reconstructed by adding the four-momenta of the $\Lambda$ and $\gamma$ to yield an invariant mass for the pair. This is done for every possible $\Lambda$ $\gamma$ combination within each event. Only one cut is imposed, which places a minimum value on the helicity angle[3] of the photon. The cut imposed is $\cos(\Theta_{hel}) \geq -0.4$. This was chosen, using DELPHI simulation, as the angle beyond which the efficiency to reconstruct the $\Sigma^0$ becomes negligible.

## 4.5 Inclusive $\Sigma^0$ Production in $q\overline{q}$ Events

The measured $\Sigma^0$ momentum range is 2 to 22 GeV/$c$, outside of which the efficiency for reconstruction is essentially zero. This measurement covers an estimated $\sim$66% of the total $\Sigma^0$ production, with $\sim$30% being below 2 GeV/$c$ and $\sim$4% above 22 GeV/$c$. This extends the previously measured fraction by a significant amount ($\sim$25%), and the efficiency over the entire range has been increased [8].

The measurement comprises the differential production rate of the $\Sigma^0$ in three momentum bins.

---

[3] the helicity angle, $\Theta_{hel}$, is the angle between $\Sigma^0$ trajectory in the lab and the $\gamma$ direction in the $\Sigma^0$ frame of reference.

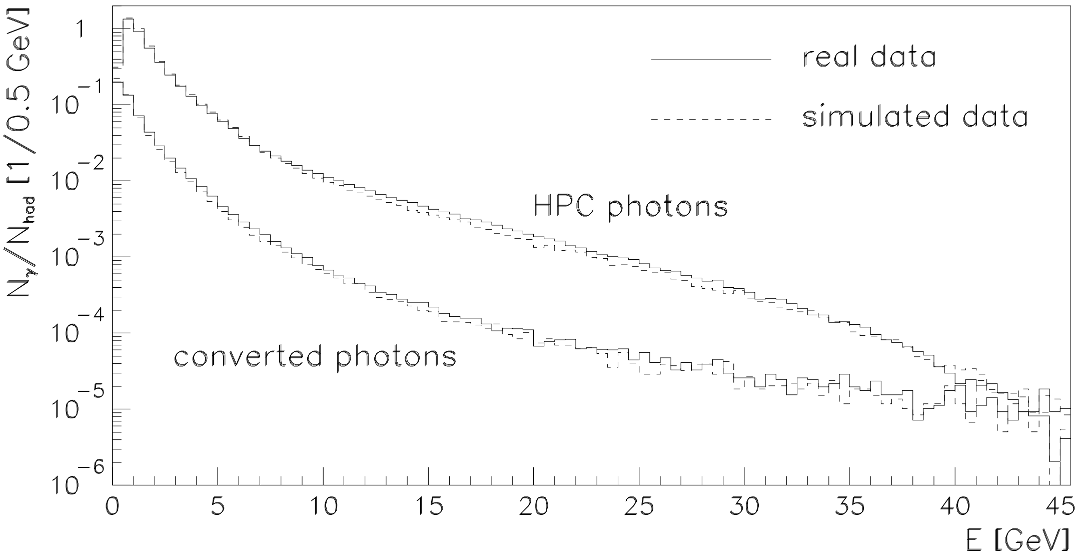

Figure 4.3 Comparison of the energy spectra of converted and calorimetric photons for real and simulated data. The number of photons is normalized to the number of events [7]

The efficiency of reconstruction in each $x_p$ bin is evaluated separately for each year using simulation. The results from each year are combined in a weighted procedure. The weights depend upon the number of data and simulation events in a given year, and the number of $\Sigma^0$'s successfully reconstructed in simulation. The data samples with a better-determined efficiency from simulation receive a larger weight.

The branching ratio calculation, with the efficiency, $\epsilon_{corr}$, corresponding to the corrected efficiency in data (Table 4.2), is given by

$$BR_{year} = \frac{1}{N_{had}(DATA)} \cdot \frac{N^{rec}_{\Sigma^0}(DATA)}{\epsilon_{corr}} = \frac{N^{rec}_{\Sigma^0}(DATA)}{N_{had}(DATA)} \cdot \frac{N^{gen}_{\Sigma^0}(MC)}{a \cdot N^{rec}_{\Sigma^0}(MC)} = R_d \cdot R_m \qquad (4.1)$$

The correction factor, $a$, is obtained from simulation and data as discussed in section 4.2. The correction is based on a large sample of protons tagged by RECV0. It accounts for differences mainly due to actual RICH performance for finding $\Lambda$'s with the extended method.

The branching ratio calculation leads to a variance $\sigma^2$, when the method of counting statistics is used and first order terms are kept

Table 4.2 Table of $\Sigma^0$ reconstruction efficiency in simulation ($\epsilon_{sim}$) and corrected efficiency in data ($\epsilon_{corr}$). The measurement is performed in the $x_p$ bins shown in bold

| | $\epsilon_{sim}$ | | | | |
|---|---|---|---|---|---|
| $x_p$ | *RECV0* | *extended* | *total* | a | $\epsilon_{corr} = a \cdot \epsilon_{sim}$ |
| 0.000 - 0.022 | 0.0000 | 0.0000 | 0.0000 | 1.0 | 0.0000 |
| 0.022 - 0.044 | 0.0001 | 0.0000 | 0.0001 | 1.0 | 0.0001 |
| **0.044 - 0.10** | **0.0012** | **0.0000** | **0.0012** | **1.0** | **0.0012** |
| **0.10 - 0.18** | **0.0030** | **0.0008** | **0.0038** | **0.95** | **0.0036** |
| **0.18 - 0.49** | **0.0024** | **0.0012** | **0.0036** | **0.94** | **0.0034** |
| 0.49 - 1.0 | 0.00005 | 0.00020 | 0.00025 | 0.48 | 0.00012 |

$$\sigma^2 \;=\; R_d^2 \cdot \sigma_m^2 + R_m^2 \cdot \sigma_d^2 \;\simeq\; R_d^2 \cdot \left( \frac{R_m^2}{a \cdot N^{rec}_{\Sigma^0}(MC)} \right) + R_m^2 \cdot \left( \frac{R_d}{N_{had}(DATA)} \right) \tag{4.2}$$

The weights used, which are $1/\sigma$, for each $x_p$ bin in each year are given by

$$Weight_{year} \;=\; \frac{\epsilon_{corr}}{\sqrt{a \cdot N^{rec}_{\Sigma^0}(MC)}} \cdot \left( \frac{N_{had}(MC)}{\frac{1}{N_{had}(MC)} + \frac{1}{N_{had}(DATA)}} \right)^{\frac{1}{2}} \tag{4.3}$$

Several methods were evaluated to obtain the best measurement of the $\Sigma^0$ differential cross section. Two methods are used to obtain the shape of the background in the $\Lambda$ - $\Lambda\ \gamma$ invariant mass spectra. For the first method, the background shape is generated by taking a $\Lambda$ from one event and placing it into another event. The second method uses the shape from simulation and applies that to data, with one parameter left free to scale to the level of background. The cut on helicity angle is also varied through the range $-0.9 \geq \cos(\Theta_{hel}) \geq -0.1$, where almost no change in efficiency occurs. This allows the background to vary, while keeping the actual $\Sigma^0$ signal constant.

In addition to having two methods of background parameterization, two methods are used to fit the invariant mass peak in an effort to determine the mean value and the error in the fit procedure. The signal peak is fit using either a single gaussian with all parameters free, or a sum of two gaussians constrained by a fit to the true $\Sigma^0$ signal in simulation. In the case of the unconstrained fit to the $\Sigma^0$ signal, the measured mean Q-value for the $\Sigma^0$ decay may be compared to the known Q-value of 76.8 MeV/$c^2$. Both simulation and data are shown to be in good agreement with this value. The differential cross section is obtained by taking the mean value of the fit to background-subtracted histograms in each $x_p$ bin. A total of eight measurements are made in each $x_p$ bin using the two signal shapes for four values of helicity angle. The use of two descriptions of background shape brings the total number of measurements in each momentum bin to sixteen. The systematic error on the fit is estimated by taking the standard deviation of results of the various fits. The mean value gives the measured differential cross section for that bin.

The differential cross section is calculated as

$$\frac{1}{\sigma_{had}}\frac{d\sigma}{dx_p} = \frac{1}{N_{had}(DATA)} \cdot \frac{N^{rec}_{\Sigma^0}(DATA)}{\Delta x_p} \cdot \frac{1}{\epsilon_{corr}} \tag{4.4}$$

where $N^{rec}_{\Sigma^0}$ is the number of reconstructed $\Sigma^0$'s in the $x_p$ bin.

The systematic uncertainties in the differential $\Sigma^0$ cross section arise from the fit procedures, the $\Lambda$ reconstruction efficiencies via the standard and extended methods, and corrections of remaining differences between data and simulation such as the material distribution within DELPHI and the energy resolution for converted photons [7]. The various contributions are summarized in Table 4.3 and are estimated as follows:

- As shown in Fig. 4.2, the material distribution is not correctly described in the simulation program. The radiation length was varied by 4% for $\gamma$ conversions occurring in front of the TPC.
- The DELPHI $\pi^0$ paper provides a relevant analysis of the error due to the reconstruction algorithms of converted photons [7]. In that analysis, only the 'best' measured converted photons (those which were reconstructed by two TPC tracks) were selected and compared to the result using all converted photons. The systematic error represents the difference between the two results.
- the error for the $\Lambda$ reconstruction algorithms is discussed in this chapter.
- the error for the fit to the $\Sigma^0$ invariant mass spectrum is discussed in the preceding paragraph.

Table 4.4 gives a break-down of the statistical and systematic contributions to the error in each $x_p$ bin.

Table 4.3 Systematic errors

| Source of systematic error | Errors (in %) |
|---|---|
| photon efficiency | 4 |
| material distribution | 3 |
| $\Lambda$ reconstruction algorithms | 7 |
| fit to $\Sigma^0$ invariant mass spectrum | 11 |
| errors added in quadrature | 14 |

Table 4.4  Statistical and systematic errors

| | Error (in %) | | | |
|---|---|---|---|---|
| | bin 1 | bin 2 | bin 3 | all bins |
| total systematic | 14.8 | 16.4 | 18.2 | 14.0 |
| statistical | 14. | 11. | 14. | 8.0 |
| sum in quadrature | 20. | 20. | 23. | 16. |

Figs. 4.4 to 4.7 show typical fits to the invariant mass spectrum for the Q-value, or the $\Lambda\gamma - \Lambda$ invariant mass, of the $\Sigma^0$ decay. Comparing the figures, one finds that the background shape in data is well-described by simulation.

One important finding of this analysis is the first differential cross section measurement of the $\Sigma^0$ in $e^+e^- \rightarrow q\bar{q}$ events, which allows a production 'shape' comparison with model predictions. The result of the differential $\Sigma^0$ cross section measurement is reported in Table 4.5.

Table 4.5  The scale-invariant differential cross sections for inclusive $\Sigma^0$ production in multi-hadronic events at $\sqrt{s} = 91.2\ GeV$

| $x_p$ | $\frac{1}{\sigma_{had}}\frac{d\sigma}{dx_p} \pm \Delta_{stat} \pm \Delta_{syst}$ |
|---|---|
| $0.044 - 0.100$ | $0.492 \pm 0.069 \pm 0.073$ |
| $0.100 - 0.180$ | $0.218 \pm 0.024 \pm 0.035$ |
| $0.180 - 0.490$ | $0.057 \pm 0.008 \pm 0.010$ |
| $0.044 - 0.490$ | $0.152 \pm 0.012 \pm 0.021$ |

Extrapolation into the non-accessible momentum regions is done using the shape predicted by JETSET 7.3. JETSET 7.3 (DELPHI tuned) predicts that ~ 34% of all $\Sigma^0$ decays occur outside the measured $x_p$ range, while JETSET 7.4 (default values) predicts ~32%, and HERWIG 5.7 predicts ~35%. The systematic error for the extrapolation is estimated to be ~ 7%. Fig. 4.8 shows the predictions of JETSET 7.4 (default values) and HERWIG 5.7, and the results of the measurement in data. The differential cross section from JETSET 7.3 (tuned) for all multi-hadronic events is shown in Fig. 4.9, along with the measurement in data.

The second, and final, important result of this analysis comes from the extrapolation using simulation (described above), which yields the production rate of $\Sigma^0$ in $Z^0$ decays. The average number of $\Sigma^0$'s produced per $Z^0$ decay is calculated to be

$$N(\Sigma^0)/Z^0_{had} = 0.101 \pm 0.008(\mathrm{stat}) \pm 0.014(\mathrm{syst}) \pm 0.007(\mathrm{extrap}) \tag{4.5}$$

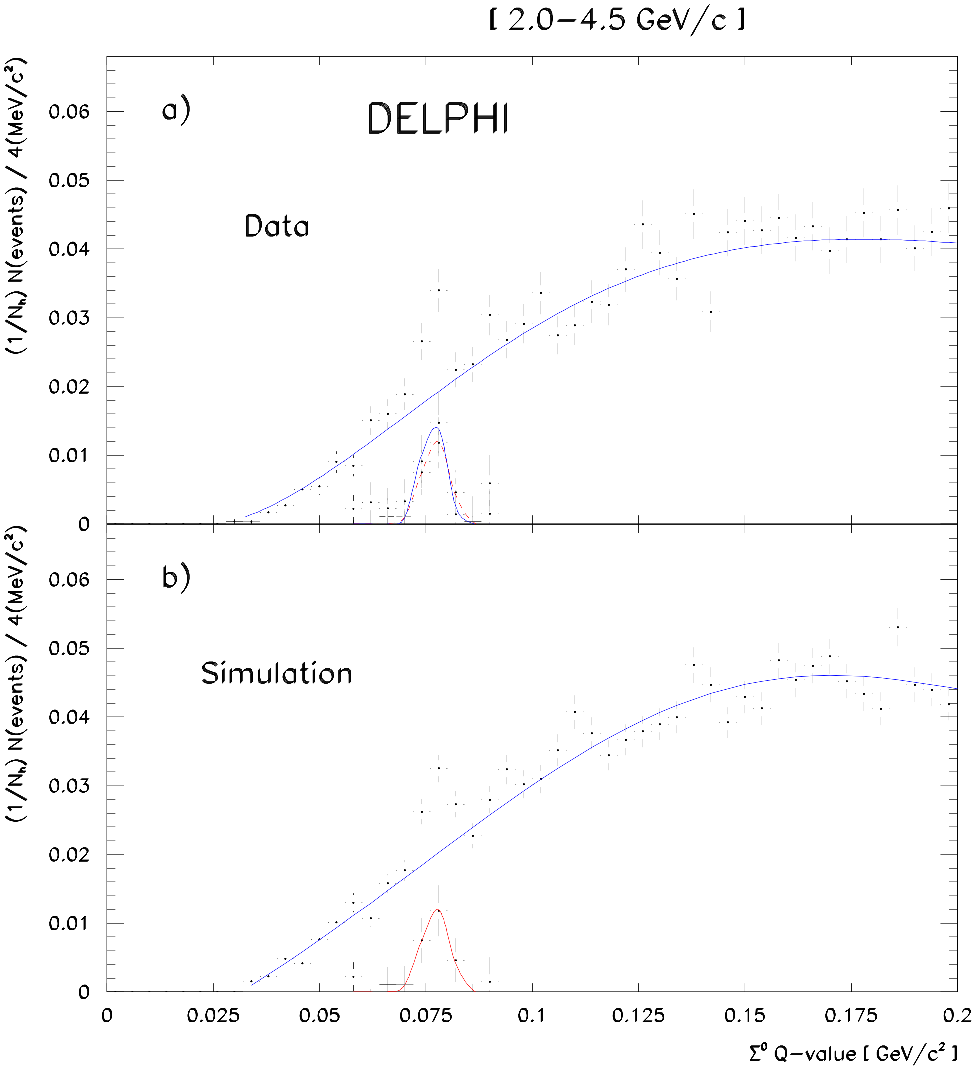

Figure 4.4 A typical fit to the $\Lambda\gamma - \Lambda$ invariant mass, bin 1
a) The data is shown by points with error bars; the line corresponds to the fit to background. The background-subtracted histogram from data is shown with a solid line for the fit to the signal. The corresponding signal from simulation is shown for comparison
b) The simulation is shown by points with error bars; the solid line corresponds to the fit to background

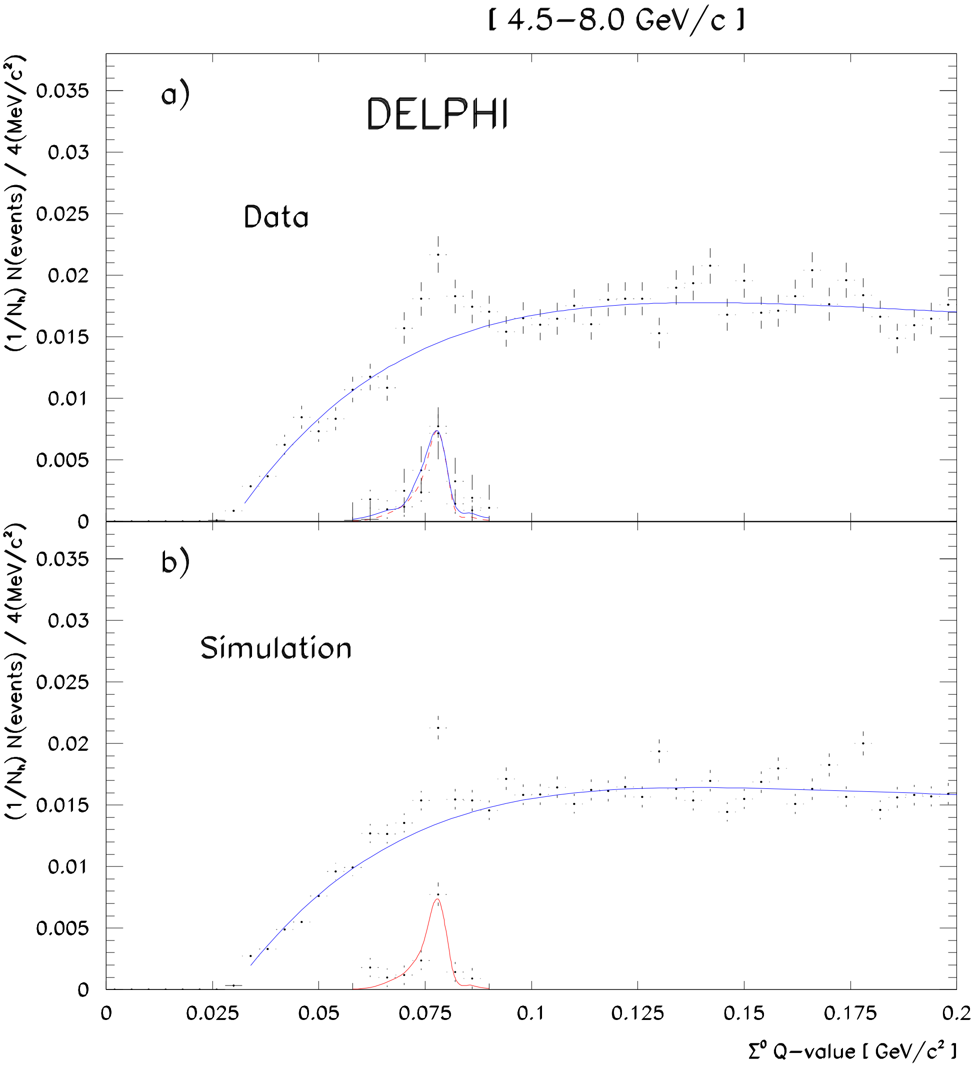

Figure 4.5 A typical fit to the $\Lambda\gamma - \Lambda$ invariant mass, bin 2
a) The data is shown by points with error bars; the line corresponds to the fit to background. The background-subtracted histogram from data is shown with a solid line for the fit to the signal. The corresponding signal from simulation is shown for comparison
b) The simulation is shown by points with error bars; the solid line corresponds to the fit to background

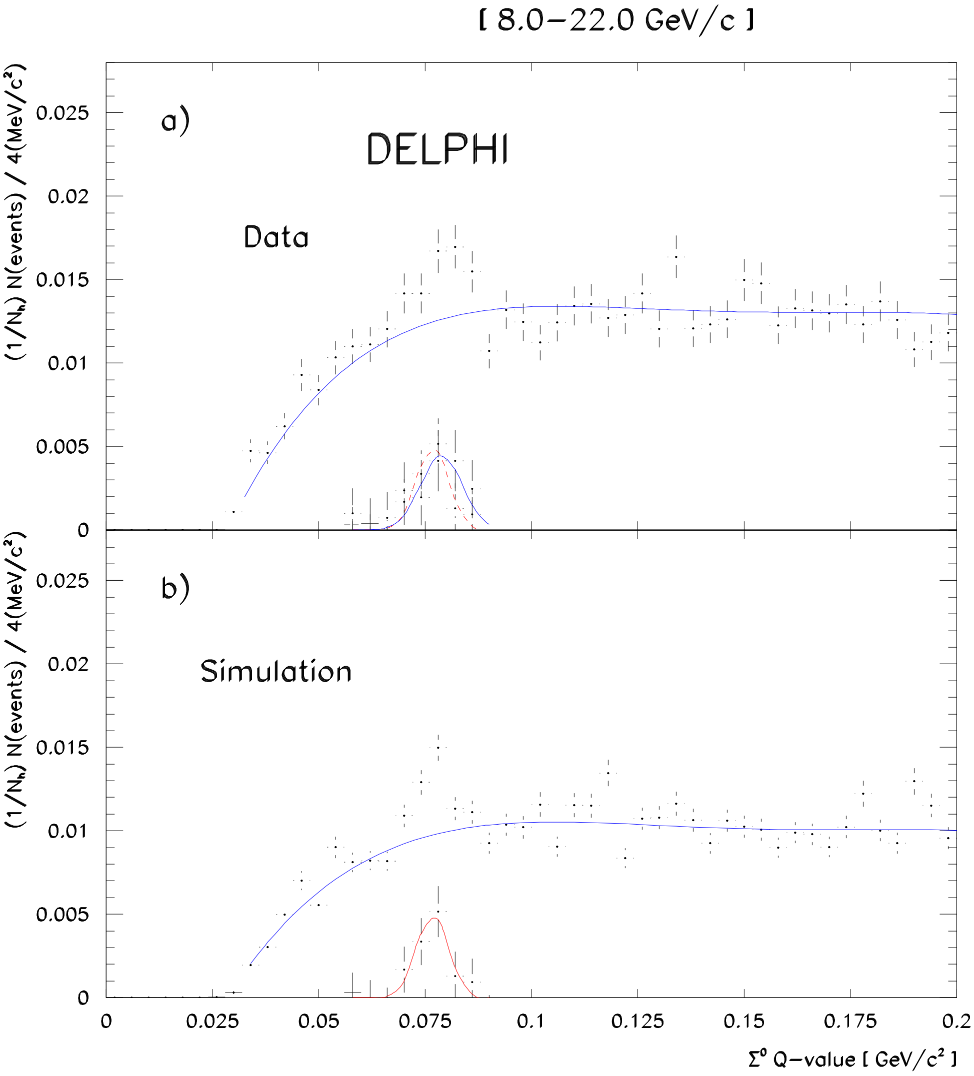

Figure 4.6 A typical fit to the $\Lambda\gamma - \Lambda$ invariant mass, bin 3
a) The data is shown by points with error bars; the line corresponds to the fit to background. The background-subtracted histogram from data is shown with a solid line for the fit to the signal. The corresponding signal from simulation is shown for comparison
b) The simulation is shown by points with error bars; the solid line corresponds to the fit to background

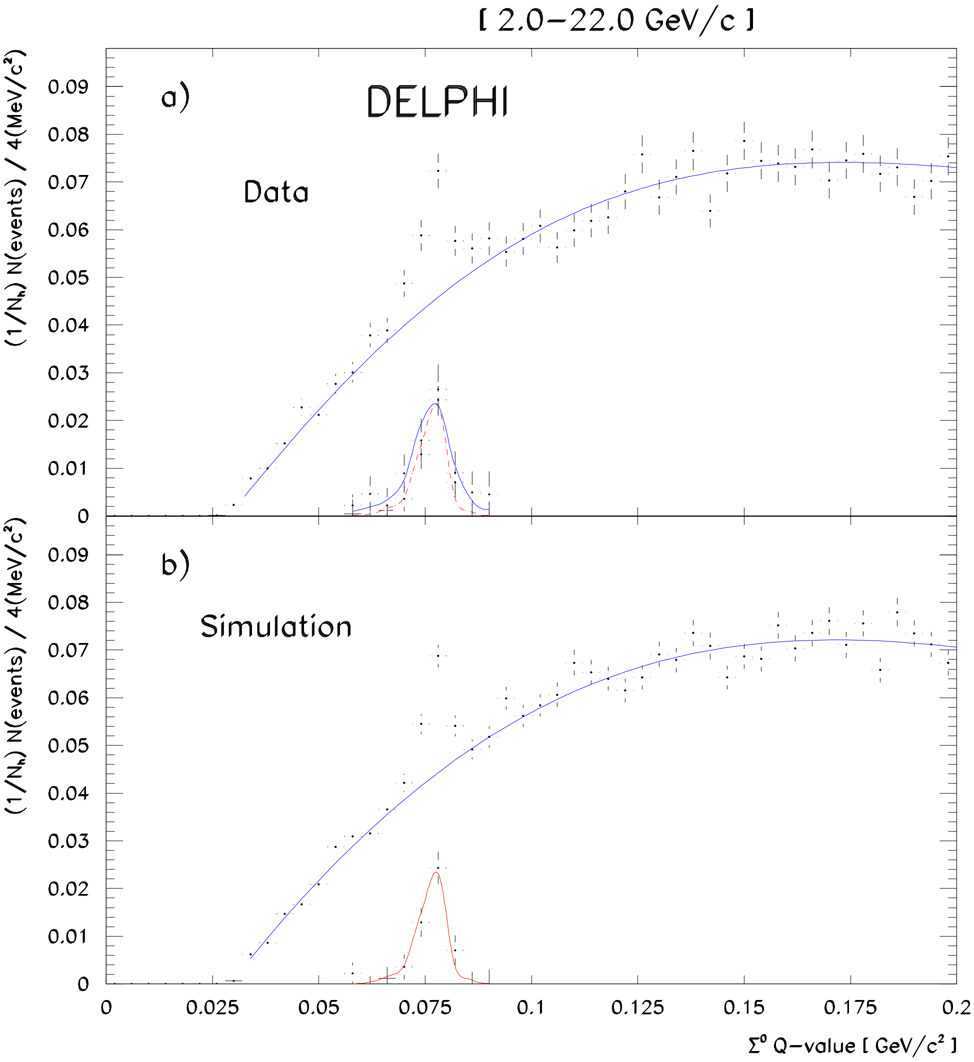

Figure 4.7 A typical fit to the $\Lambda\gamma - \Lambda$ invariant mass for entire measured $x_p$ range
a) The data is shown by points with error bars; the line corresponds to the fit to background. The background-subtracted histogram from data is shown with a solid line for the fit to the signal. The corresponding signal from simulation is shown for comparison
b) The simulation is shown by points with error bars; the solid line corresponds to the fit to background

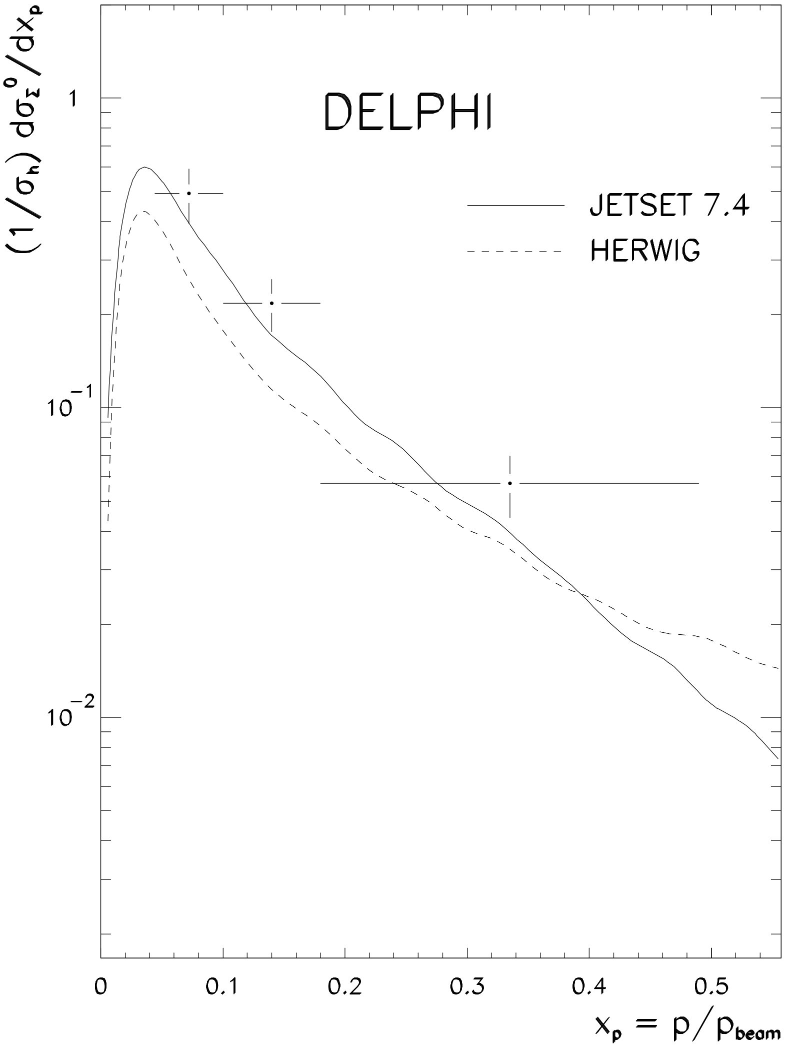

Figure 4.8 Measured differential cross section for $\Sigma^0$ at $\sqrt{s} = 91.2\ GeV$ (data points), and the prediction of the models with default tuning. The curves are not smooth due to limited MC statistics

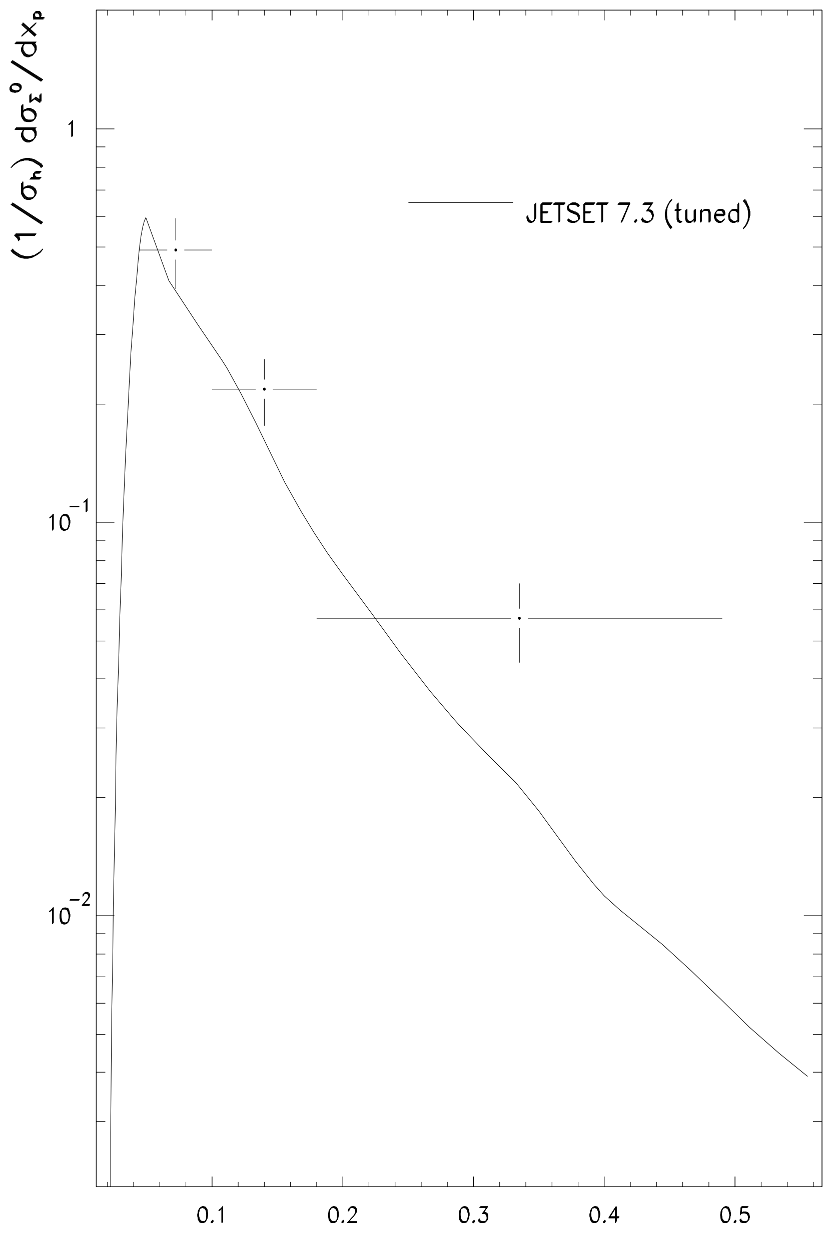

Figure 4.9 Measured differential cross section for $\Sigma^0$ at $\sqrt{s} = 91.2\ GeV$ (data points), and the JETSET 7.3 (tuned) model prediction. The curve is not smooth due to limited MC statistics

# 5 SUMMARY

*He had been eight years upon a project for extracting sunbeams out of cucumbers, which were to be put in vials hermetically sealed, and let out to warm the air in raw inclement summers.*

Jonathan Swift (1667-1745) (*Gulliver's Travels*)

This thesis presents a measurement of the production rate of the $\Sigma^0$ hyperon. It is one of the three isospin states of the $J^P = \frac{1}{2}^+$ octet $\Sigma$ baryons. In addition, the analysis yields the first differential cross-section measurement of the $\Sigma^0$ hyperon in $e^+e^- \to q\bar{q}$ events. These results are a correction to the measurement of the inclusive $\Sigma^0$ production rate found in my previous analysis [8]. The main differences between the two analyses, which have led to a correction, include:

- a less restrictive cut on the helicity angle, $\Theta_{hel}$, of the $\gamma$
- a wider cut on the invariant mass of the $\Lambda$ candidate
- no pion rejection on the leading track of the $\Lambda$ candidate
- efficiencies are calculated more carefully on a year-by-year basis
- efficiency of reconstruction in each $x_p$ bin is evaluated separately for both simulation and data
- background levels in data are not required to match those in simulation

The average number of $\Sigma^0$'s produced per $Z^0$ decay is calculated to be

$$N(\Sigma^0)/Z^0_{had} = 0.101 \pm 0.008(\text{stat}) \pm 0.014(\text{syst}) \pm 0.007(\text{extrap}) \tag{5.1}$$

The $\Sigma^0$ production rate found here is incompatible with HERWIG at the 2.5 $\sigma$ level, but is within 2 $\sigma$ of the prediction of JETSET .

The results of the differential $\Sigma^0$ cross section measurement are reported in Table 4.5 and shown in Figs. 4.8 and 4.9. Within errors, the shape of the $x_p$ distribution is described by both JETSET and HERWIG .

Table 5.1 summarizes the measured and predicted rates of the $J^P = \frac{1}{2}^+$ octet $\Sigma$ baryons. The inclusive rates of the three isospin states of the $J^P = \frac{1}{2}^+$ octet $\Sigma$ baryons have all been measured, and are found to be higher than the predicted values in each case.

A broader comparison with model predictions may be made by including other octet and decuplet mass states. The ARGUS collaboration has a good discussion of the strangeness and spin suppression effect in the fragmentation process [11], and they include a number of references. In Fig. 5.1a, the strangeness suppression in baryon production is determined by the production ratio of hyperons which differ by one unit in strangeness. Another symmetry-breaking effect in the fragmentation process can be studied by comparing the production of octet and decuplet baryons with the same flavor content. Fig. 5.1b shows the spin suppression for two such ratios. Both DELPHI and ARGUS results are included, along with the JETSET 7.3 (tuned) and HERWIG 5.7 model predictions. It shows that there is good agreement between the results of ARGUS and DELPHI. It also illustrates the inability of the (simpler) HERWIG model to describe strange baryon production.

Table 5.1 Previously published measurements of $\Sigma^0$,$\Sigma^-$, and $\Sigma^+$ production, and predictions of JETSET and HERWIG . Statistical and systematic errors have been added in quadrature

| Source | $\sqrt{s}$ (GeV) | $< \Sigma^0 + \overline{\Sigma^0} >$ | $< \Sigma^- + \overline{\Sigma^-} >$ | $< \Sigma^+ + \overline{\Sigma^+} >$ | ref |
|---|---|---|---|---|---|
| ARGUS | 10 | $0.023 \pm 0.008$ | – | – | [11] |
| DELPHI | 91 | – | $0.081 \pm 0.013$ | – | [46] |
| OPAL | 91 | $0.071 \pm 0.018$ | $0.083 \pm 0.011$ | $0.099 \pm 0.015$ | [6] |
| this analysis | 91 | $0.101 \pm 0.016$ | – | – | – |
| JETSET | 91 | 0.073 | 0.067 | 0.072 | – |
| HERWIG | 91 | 0.056 | 0.060 | 0.069 | – |

To conclude with what was discussed in the introduction, the comparison here between measurements and model predictions is an attempt to better understand the underlying physics of QCD processes such as fragmentation. The mechanism of baryon production in JETSET is somewhat different from that of HERWIG , and we have seen that in the case of strange baryon production, HERWIG has difficulty. The DELPHI Collaboration uses JETSET 7.3, tuned to results from data, as the generator of physics events which are put through the detector simulation. In the strange sector, the observables used to tune the model are:

- Average multiplicity of $\Omega^-$, $\Xi^-$, $\Sigma^*(1385)$, $\phi$, and $K^*(892)$

- $K^0$ differential cross section
- $\Lambda$ differential cross section
- $\Lambda\,\overline{\Lambda}$ multiplicity

from DELPHI and OPAL. With the adjustment of a large number of parameters, the model is able to approach a good description of many features of strange meson and baryon production which are input for the iterative tuning procedure. Significant differences do exist, however, and one would hope for a simpler description with better overall agreement before we can say that we understand the process of hadronization.

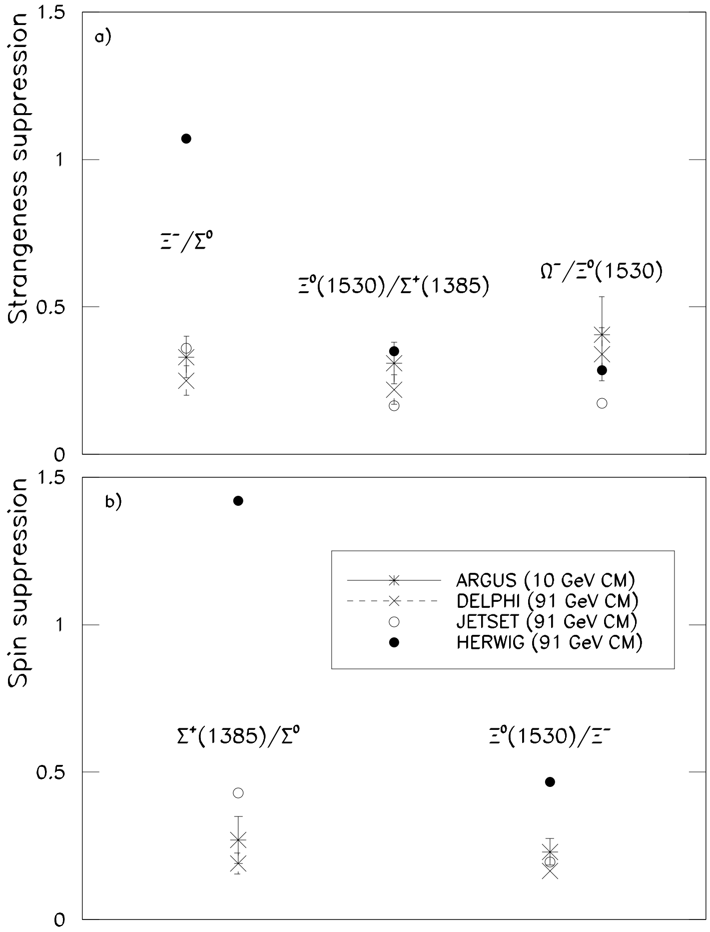

Figure 5.1 a) Strangeness suppression determined from hyperon production rates

b) Spin 3/2 suppression determined from hyperon production rates

# BIBLIOGRAPHY

[1] DELPHI Collaboration, P. Abreu *et al.*, Z. Phys. **C 54** (1992) 55

[2] DELPHI Collaboration, P. Abreu *et al.*, Z.Phys. **C67** (1995) 543; Z.Phys. **C70** (1996) 371

[3] DELPHI Collaboration, P. Abreu *et al.*, Phys. Lett. **B 334** (1994) 435

[4] DELPHI Collaboration, P. Abreu *et al.*, Z. Phys. **C 68** (1995) 353

[5] DELPHI Collaboration, P. Abreu *et al.*, Nucl. Instrum. Meth. **A378** (1996) 57

[6] OPAL Collaboration, P.D. Acton *et al.*, Phys.Lett. **B291** (1992) 503

[7] DELPHI Collaboration, W. Adam *et al.*, Z. Phys. **C69** (1996) 561

[8] DELPHI Collaboration, W. Adam *et al.*, Z. Phys. **C 70** (1996) 371-382

[9] T.J. Adye, A. Augustinus, M. Donszelmann, T. Rovelli, R.L. Sekulin, G.R. Smith, Nucl. Instrum. Meth. **A349**(1994) 160

[10] ARGUS Collaboration, H. Albrecht *et al.*, Phys. Lett. **183B** (1987) 419;
ARGUS Collaboration, H. Albrecht *et al.*, Z. Phys. **C9** (1988) 177

[11] ARGUS Collaboration, H. Albrecht *et al.*, Z.Phys. **C39** (1988) 177

[12] OPAL Collaboration, G. Alexander *et al.*, CERN-PPE/96-99 (1996)

[13] B. Anderson, G. Gustavson, G. Ingelman, T. Sjöstrand, Phys. Rep. **97** (1983) 31

[14] G. Van Apeldoorn *et al.*, *Performance of the Barrel Ring Imaging Cherenkov Counter of DELPHI*, DELPHI-Note 94-18 RICH 61 (1994)

[15] L. Arnaudon *et al.*, CERN-SL/93-20I-DI, Washington 1993 Particle Accelerator Conference (PAC 93) (1993) 44-46

[16] X. Artru, G. Mennessier, Nucl. Phys. **B 70** (1974) 93;
G.C. Fox, S. Wolfram, Nucl. Phys. **B 168** (1980) 285;
R. Field, S. Wolfram, Nucl. Phys. **B 213** (1983) 65

[17] Jade Collaboration, W. Bartel *et al.*, Phys. Lett. **B 101** (1981) 129

[18] DELPHI Collaboration, W. Bartl *et al.*, *DELPHI Technical Proposal*, CERN-LEPC/83-3 (1983);
DELPHI Collaboration, Nucl. Instr. Meth. **A 303** (1991) 233

[19] F.A. Behrends, W. Hollik, R. Kleiss, Nucl. Phys. **B 304** (1988) 712

[20] N. Bingefors *et al.*, Nucl. Instr. Meth. **A 328** (1993) 447;
V. Chabaud *et al.*, *The DELPHI Silicon Strip Microvertex Detector with Double Sided Readout*, CERN-PPE/95-86 (1995)

[21] M. Blume, E. Schyns *Study of Baryon Production with* $\Lambda$ *Baryons and Protons* DELPHI-Note 96-75 CONF 7, 1996

[22] DELPHI trigger Group, V. Bocci *et al.*, Nucl. Instrum. Meth. **A362**(1995) 361

[23] W. de Boer, H. Fürstenau, *Comparison of DELPHI data with QCD models*, DELPHI-Note 91-75 PHYS 129;
K. Hamacher, M. Weierstall, *The Next Round of Hadronic Generator Tuning Heavily Based on Identified Particle Data*, DELPHI-Note 95-80 PHYS 515

[24] G. Borisov, DELPHI-Note 94-125 PROG 208 (1994)

[25] B. Bouquet, P. Gavillet, J.-P. Laugier, DELPHI-Note 93-29 DAS 141 (1993)

[26] C. Bourdarius *et al.*, *User guide of the HADIDENT/RICH software*, 8 August 1995, unpublished;
C. Bourdarius *et al.*, *A few plots about the barrel RICH performance*, 23 July 1995, unpublished

[27] K. Brand, M. Feindt, C. Kreuter, O. Podobrin, *ELEPHANT Users Manual*, DELPHI-Note in preparation

[28] R. Brun *et al.*, CERN report DD/EE/84-1 (1986)

[29] J.E. Campagne, R. Zitoun, Z. Phys. **C 43** (1989) 469

[30] CERN accelerator division (SL), LEP statistics, http://nicewww.cern.ch/sl/stat/lucompar.gif (1995)

[31] DELPHI Collaboration, *DELPHI Data Analysis Program (DELANA) User's Guide*, DELPHI-Note 89-44 PROG 137 (1989)

[32] DELPHI Collaboration, *DELSIM – DELPHI Event Generation and Detector Simulation*, DELPHI-Note 89-15 PROG 130 (1989)

[33] DELPHI Collaboration, *Proposal for the DELPHI Surround Muon Chambers* DELPHI-Note 92-139 TRACK 71 (1992);
DELPHI Collaboration, *Proposal for the Replacement of the Small Angle Calorimeter of DELPHI*, CERN-LEPC/92-6 (1992);
S.J. Alvsvaag *et al.*, *The DELPHI Small Angle Tile Calorimeter*, DELPHI-Note 94-157 CAL 120 (1994)

[34] M. Feindt, W. Oberschulte gen. Beckmann, C. Weiser *How to use the MAMMOTH program* DELPHI-Note 96-52 PROG, 1996

[35] B. Franek *et al.*, *Architecture of the DELPHI on-line Data Acquision Control System*, DELPHI-Note 92-104 DAS 130 (1992)

[36] V. Hatten *et al.*, LEP Performance Note 12 (1990);
R. Baily *et al.*, CERN-SL/90-95 (1990)

[37] S. Jadach *et al.*, Comp. Phys. Comm. **79** (1994) 503

[38] C. Kreuter, Diploma Thesis, IEKP-KA/93-9 (1993)

[39] G. Marchesini et. al., Computer Physics Communications **67** (1992) 465

[40] G. Marchesini *et al.*, Comp. Phys. Comm. **67** (1992) 465

[41] W.R. Nelson *et al.*, *EGS4 User Manual*, SLAC-265 (1985)

[42] Y. Sacquin, Version 3.15, DELPHI-Note 94-161 PROG 210 (1994)

[43] E. Schyns, *NEWTAG - $\pi$, K, p Tagging for Delphi RICHes* DELPHI-Note 96-103 RICH, 1996

[44] T. Sjöstrand, PYTHIA *5.6 and* JETSET *7.3 Physics and Manual*, CERN-TH. 6488/92

[45] T. Sjöstrand, Comp. Phys. Comm. **39** (1986) 347;
T. Sjöstrand, M. Bengtsson, Comp. Phys. Comm. **43** (1987) 367;
T. Sjöstrand, Comp. Phys. Comm. **82** (1994) 74

[46] C. Weiser, M. Feindt $\Sigma^-$*Production in Hadronic* $Z^0$ *Decays* DELPHI-Note 96-69 CONF 3, 1996

# ACKNOWLEDGEMENTS

*I have never let my schooling interfere with my education.*

Mark Twain (1835-1910)

I would like to acknowledge the valuable support of my advisor, Dr. Bert Crawley. His contribution to the process of obtaining a Ph.D. has spanned four years, and it has truly been a pleasure working with him. The members of the ELEPHANT, MAMMOTH, and HADIDENT tasks also provided technical support in this endeavor. Indispensible help and guidance was generously provided by Dr. Tony Hill, Dr. Michael Feindt, and Dr. Emile Schyns.

My wife, Christine, has also provided capable and loving support in this adventure. Her uncontrollable urge to yawn upon the first utterance of any physics topic, a contradistinction to her usual propensity toward grandiloquence, has not in any way diminished her role in the eventual completion of the thesis and the Ph.D.